

Centennial-Scale Variability of Terrestrial Near-Surface Wind Speed over China from Reanalysis

CHENG SHEN,^a JINLIN ZHA,^{b,c} JIAN WU,^c AND DEMING ZHAO^b

^a *Gaochun Meteorological Bureau, Nanjing, China*

^b *CAS Key Laboratory of Regional Climate and Environment for Temperate East Asia, Institute of Atmospheric Physics, Chinese Academy of Sciences, Beijing, China*

^c *Key Laboratory of Atmospheric Environment and Processes in the Boundary Layer over the Low-Latitude Plateau Region, Department of Atmospheric Science, Yunnan University, Kunming, China*

(Manuscript received 6 June 2020, in final form 20 March 2021)

ABSTRACT: Investigations of variations and causes of near-surface wind speed (NWS) further understanding of atmospheric changes and improve the ability of climate analysis and projections. NWS varies on multiple temporal scales; however, the centennial-scale variability in NWS and associated causes over China remains unknown. In this study, we employ the European Centre for Medium-Range Weather Forecasts (ECMWF) Twentieth Century Reanalysis (ERA-20C) to study the centennial-scale changes in NWS from 1900 to 2010. Meanwhile, a forward stepwise regression algorithm is used to reveal the relationships between NWS and large-scale ocean–atmosphere circulations. The results show three unique periods in annual mean NWS over China from 1900 to 2010. The annual mean NWS displayed decreasing trends of -0.87% and -11.75% decade⁻¹ from 1900 to 1925 and from 1957 to 2010, respectively, which were caused by the decreases in the days with strong winds, with trends of -6.64 and -4.66 days decade⁻¹, respectively. The annual mean NWS showed an upward trend of 55.47% decade⁻¹ from 1926 to 1956, which was caused by increases in the days with moderate (0.43 days decade⁻¹) and strong winds (23.55 days decade⁻¹). The reconstructed wind speeds based on forward stepwise regression algorithm matched well with the original wind speeds; therefore, the decadal changes in NWS over China at the centennial scale were mainly induced by large-scale ocean–atmosphere circulations, with the total explanation power of 66%. The strongest explanation power was found in winter (74%), and the weakest explanation power was found in summer (46%).

KEYWORDS: Extreme events; Wind; Climate variability; Climatology; Surface temperature; Trends

1. Introduction

Near-surface wind speed (NWS) is an important parameter in the study of atmospheric dynamics and climate change and has a considerable effect on wind energy (Li et al. 2008; Zhang et al. 2009; He et al. 2010), visibility (Zhang et al. 2015), evapotranspiration (Niyogi et al. 2011; McMahon et al. 2013), and soil moisture (Liu et al. 2014). Therefore, many studies have looked at how NWS changes at global and regional scales (Vautard et al. 2010; Azorin-Molina et al. 2014, 2018; Zeng et al. 2019).

Numerous studies have shown that NWS has been decreasing at the global scale since the 1960s (McVicar et al. 2012; Wu et al. 2018a), especially for the midlatitude regions of the Northern Hemisphere (Peterson et al. 2011; Tobin et al. 2014; Berrisford et al. 2015; Zhang et al. 2019). A reduction in NWS has also been observed at a regional scale, including in Australia from 1975 to 2006 (McVicar et al. 2008), Czech Republic from 1961 to 2005 (Brazdil et al. 2009), Switzerland

from 1983 to 2006 (McVicar et al. 2010), United States from 1971 to 2000 (Greene et al. 2012), United Kingdom from 1980 to 2010 (Earl et al. 2013), Turkey from 1975 to 2006 (Dadaser-Celik and Cengiz 2014), South Korea from 1954 to 2003 (Kim and Paik 2015), Spain and Portugal from 1961 to 2014 (Azorin-Molina et al. 2016), and Brazil from 1980 to 2014 (Gilliland and Keim 2018). A slowdown in NWS was also observed in China over the last 50 years (Zheng et al. 2009; Jiang et al. 2010; Guo et al. 2011; Lin et al. 2013; Liu et al. 2014; Li et al. 2018; Zha et al. 2019a). Roderick et al. (2007) termed these declining trends in NWS as “stilling.” Furthermore, many studies also compared the NWS in reanalysis products with observations to estimate its climatology, interannual variability, and trends (Torralba et al. 2017; Ramon et al. 2019; Wohland et al. 2019). However, the decreasing trends in all reanalysis products were weaker than observations (You et al. 2010; Chen et al. 2014; Wu et al. 2016; Zha et al. 2017; Zhang and Wang 2020). Nevertheless, the spatiotemporal characteristics of NWS at the centennial scale have yet to be revealed over China.

The causes of terrestrial stilling include large-scale and regional-scale factors (McVicar et al. 2012; Wu et al. 2018a). The large-scale factors involve changes in large-scale ocean–atmosphere circulations (LOACs). In China, the predominant LOACs that affect NWS include the East Asian monsoons (Xu et al. 2006), the Pacific decadal oscillation (PDO; Fu et al. 2011), El Niño–Southern Oscillation (ENSO; Chen et al. 2013), and the Northern Hemisphere annular mode (Wu et al. 2018b). The regional-scale factors affecting NWS mainly include land-use and land-cover

Denotes content that is immediately available upon publication as open access.

Supplemental information related to this paper is available at the Journals Online website: <https://doi.org/10.1175/JCLI-D-20-0436.s1>.

Corresponding author: Jinlin Zha, zhajl@tea.ac.cn

DOI: 10.1175/JCLI-D-20-0436.1

© 2021 American Meteorological Society. For information regarding reuse of this content and general copyright information, consult the AMS Copyright Policy (www.ametsoc.org/PUBSReuseLicenses).

change (Wu et al. 2016; Zha et al. 2017, 2019b), air pollution (Xu et al. 2006), anthropogenic heat release (Zhang et al. 2017), and the instrumental drift (Thomas and Swail 2011).

Compared to the terrestrial stilling, some studies also discovered a reversal of stilling in recent decades (Kim and Paik 2015; Azorin-Molina et al. 2018; Zeng et al. 2019). For instance, NWS showed an increasing trend over southwestern China after the year 2000 (Yang et al. 2012). The upward trends of NWS reached $0.04 \text{ m s}^{-1} \text{ decade}^{-1}$ over northwestern China from 1993 to 2005 (Li et al. 2018), and $0.0008 \text{ m s}^{-1} \text{ decade}^{-1}$ over eastern China since 2000 (Zha et al. 2019a). The predominant factor of reversal in terrestrial stilling could be the LOACs (Zeng et al. 2019; Zhang and Wang 2020). Some studies also pointed out that recovery of NWS may occur in the next two decades (Zeng et al. 2019; Zha et al. 2020). Consequently, the stilling and reversal could be a cyclical, decadal pattern of NWS. However, recent studies mainly analyzed the trends in NWS over the past several decades in China, and the multidecadal characteristics in NWS and the corresponding causes have yet to be revealed.

What are the characteristics of NWS changes at the centennial scale over China? What is the predominant factor that induced the decadal changes in NWS at the century time scale over China? These issues will be analyzed in this study. The remainder of this paper is organized as follows: datasets and methods are introduced in section 2. Results are presented in section 3, and the causes of NWS changes are presented in section 4. The discussion is provided in section 5, and the conclusions are summarized in section 6.

2. Datasets and methods

a. Datasets

1) REANALYSIS OUTPUT

Continuous observations for NWS in China at the centennial scale are absent. To investigate the centennial-scale variability in NWS, reanalysis products have been the first choice for researchers. In this study, four reanalysis products with daily mean wind speed are employed, including 1) the European Centre for Medium-Range Weather Forecasts (ECMWF) Twentieth Century Reanalysis (ERA-20C) assimilating surface observations only, 2) ECMWF Twentieth Century Reanalysis with a model-only integration (ERA-20CM), 3) the ECMWF 10-member ensemble of Coupled Climate Reanalyses of the twentieth century (CERA-20C), and 4) the National Oceanic and Atmospheric Administration–Cooperative Institute for Research in Environmental Sciences (NOAA-CIRES) Twentieth Century Reanalysis, version 2c (NOAA-CIRES-20CR-V2C). ERA-20C is produced with ECMWF Integrated Forecasting System (IFS), version Cy38r1, which is ECMWF's first atmospheric reanalysis of the twentieth century for 1900–2010 (Poli et al. 2013). The assimilation methodology is 24-h 4D-var analysis. The ERA-20CM model integrations are based on a 1-h time step and $0.5^\circ \times 0.5^\circ$ horizontal resolution. No synoptic meteorological data are assimilated in ERA-20CM (Hersbach et al. 2015). CERA-20C is produced with the Integrated Forecasting System, version Cy41r2, and uses atmospheric

forcings as the final version of the atmospheric model integration, which is the ECMWF 10-member ensemble of coupled climate reanalyses of the twentieth century available for 1901–2010 (Hersbach et al. 2015). NOAA-CIRES-20CR-V2C is produced by the Earth System Research Laboratory Physical Sciences Division from NOAA and the University of Colorado CIRES and assimilates only surface observations of synoptic pressure. Products include 6-hourly ensemble mean and spread analysis fields on a $2.0^\circ \times 2.0^\circ$ global latitude–longitude grid, and 6-hourly ensemble mean and spread forecast fields (Compo et al. 2011; Hirahara et al. 2014; Giese et al. 2016). Some prior studies have used these reanalysis products to investigate climatic changes at the century time scale (Compo et al. 2006; Bett et al. 2017; Luo et al. 2019). Details for these reanalysis products are shown in Table 1.

2) ANEMOMETER OBSERVATIONS

To select the models with good performance to investigate the variability in NWS, daily mean wind speeds from China Meteorological Administration (CMA) are used. The wind speeds were measured by anemometer 10 m above ground, and the siting, installation, and observation of the anemometer conformed to the standard of the World Meteorological Organization's Guide to Global Observation System and CMA's technical regulation on weather observation (Tao et al. 1997; China Meteorological Administration 2003). This dataset has been examined and calibrated by the National Meteorological Information Center of CMA. The quality control methods used by the National Meteorological Information Center include the extreme test and the temporal consistent test. To obtain a high-quality wind speed record at each station, the stations were selected based on the following criteria: 1) the station was a national standard meteorological station, 2) the station was not relocated in the study period, and 3) the total days of missing data accounted for less than 1% of the length of total data series. With these requirements, 556 stations were selected. Homogenization of the 556 stations is described in section 2b.

3) LOACs INDICES

To investigate the possible influences of LOACs on the variability in NWS over China, following previous studies in which relationships between wind speed and climate indices (CIs) were analyzed (Azorin-Molina et al. 2014; Minola et al. 2016; Zeng et al. 2019), we selected 17 time series of CIs to assess the effects of LOACs on NWS (Table 2). These CIs exert considerable effects on climatic changes in China and are informative in terms of the decadal and multidecadal variations of LOACs, having been widely used by the climate community.

b. Methods

1) QUALITY CONTROL AND HOMOGENIZATION OF NWS

An estimation of statistical significance for the selected stations is necessary since the results are influenced considerably by the inhomogeneity of NWS (Li et al. 2011). In this study, the standard normal homogeneity test (SNHT) and Pettitt test are used, which have been extensively employed in many studies

TABLE 1. Summary of the main characteristics of the four centennial-scale global reanalysis products.

	ERA-20C	ERA-20CM	CERA-20C	NOAA-CIRES-20CR-V2C
Production center	ECMWF	ECMWF	ECMWF	NOAA-CIRES
Full name	ECMWF twentieth century assimilating surface observations only	ECMWF twentieth century atmospheric model ensemble	A coupled ECMWF twentieth century reanalysis	NOAA-CIRES Twentieth Century Global Reanalysis, version 2C
Production platform	ECMWF IFS	ECMWF IFS	ECMWF IFS	NCEP Global Forecast System (GFS) 2008ex
Spatial resolution	$0.5^\circ \times 0.5^\circ$	$0.5^\circ \times 0.5^\circ$	$0.5^\circ \times 0.5^\circ$	$2.0^\circ \times 2.0^\circ$
Temporal resolution	3-hourly	3-hourly	3-hourly	6-hourly
Assimilation system	IFS cy38r1	—	IFS cy38r1	An ensemble Kalman filter
Assimilation variables	Surface pressure Surface level pressure Surface marine wind	—	Surface pressure Surface marine wind Ocean temperature Salinity profile	Surface pressure
Temporal coverage	1900–2010	1900–2010	1901–2010	1851–2012
References	Poli et al. (2016)	Hersbach et al. (2015)	Laloyaux et al. (2018)	Compo et al. (2011)
URL	https://apps.ecmwf.int/datasets/data/era20c-daily/levtype=sfc/type=an/	https://apps.ecmwf.int/datasets/data/era20cm-edmo/levtype=sfc/	https://apps.ecmwf.int/datasets/data/cera20c/levtype=sfc/type=an/	https://rda.ucar.edu/datasets/ds131.2/

(Alexandersson 1986; He et al. 2012; Zhang et al. 2020). First, we employed the SNHT method to carry out quality control according to Eq. (1):

$$Q_i = \frac{Y_i \sum_{j=1}^n \rho_j^2}{\sum_{j=1}^n (\rho_j^2 X_{ji} \bar{Y}/\bar{X}_j)}, \quad (1)$$

where Q_i is the reference function, Y_i denotes the mean wind speed of the tested station in the year i , \bar{Y} denotes the mean value of the tested station from 1970 to 2010, X_{ji} denotes the mean wind speed of reference station j in year i , \bar{X}_j denotes the mean value of reference station j , ρ_j denotes the correlation between the tested and reference stations, and n denotes the total number of reference stations. If stations are enclosed within a circle with radius of 1° latitude and longitude centered at the tested station, the stations are selected as the reference stations (Li et al. 2003). Based on Eq. (1), a new standardized series $Z_i = (Q_i - \bar{Q})/S_Q$ can be computed, where \bar{Q} is the mean value of Q_i and S_Q is the standard deviation of Q_i . If $\{Z_i\}$ has a breakpoint, which occurs at point K ($1 \leq K \leq i$), the testing statistic $T_K = K\mu_1^2 + (i - K)\mu_2^2$ is established, where μ_1 and μ_2 denote the mean value of serial before and after breakpoint K . If the maximum value of T_K is smaller than the threshold (8.10, $p < 0.05$), the data are homogeneous (Liu 2000).

The SNHT is sensitive to the start and end points, so the Pettitt test is further used to examine the stations that passed the SNHT test. The Pettitt test is a nonparametric detection method. For a sequence X_1, X_2, \dots, X_n , its rank sequence is r_1, r_2, \dots, r_n , and the corresponding statistic S_k is defined as

$$S_k = 2 \sum_{i=1}^k r_i - k(n-1) \quad k = 1, 2, \dots, n, \quad \text{and} \quad (2)$$

$$r_i = \begin{cases} +1 & x_i > x_j \\ 0 & x_i = x_j \\ -1 & x_i < x_j \end{cases}. \quad (3)$$

If the maximum value of S_k is larger than the threshold (167, $p < 0.05$) of the Pettitt test, the corresponding i is defined as the mutation point. Based on the combination of SNHT and Pettitt test, 556 stations passed the homogenization test. (The spatial distribution of the 556 stations is shown in Fig. S1 in the online supplemental material.)

2) PIECEWISE LINEAR FUNCTION

A traditional single linear model cannot provide an adequate description of a change in a variable's tendency; therefore, we employ a piecewise linear function (PWL) to fit the trends of NWS during different periods. PWLF can automatically detect where the slope of a linear function changes and find the optimal breakpoints, allowing for multiple linear models to be fitted to each distinct section of the time series (Fyllas et al. 2009; Jekel and Venter 2019). A PWLF can be described using Eq. (4):

$$y(t) = \begin{cases} \eta_1 + m_1(t - b_1) & b_1 < t < b_2 \\ \eta_2 + m_2(t - b_2) & b_2 < t < b_3 \\ \vdots & \vdots \\ \eta_{n_b-1} + m_{n_b-1}(t - b_{n_b-1}) & b_{n_b-1} < t < b_{n_b} \end{cases}, \quad (4)$$

where b_1 is the location t of the first breakpoint, b_2 is the location t of the second breakpoint, and so forth until the last

TABLE 2. The 17 large-scale ocean–atmospheric circulation indices.

No.	Acronym	Full name	Time period	Source	References
1	AMM	Atlantic meridional mode	1948–2018	https://psl.noaa.gov/data/timeseries/monthly/AMM/ammst.data	Chiang and Vimont (2004)
2	AO	Atlantic Oscillation	1950–2018	https://psl.noaa.gov/data/correlation/ao.data	Higgins et al. (2002)
3	NAO	North Atlantic Oscillation	1948–2018	https://psl.noaa.gov/data/correlation/nao.data	Barnston and Livezey (1987)
4	PDO	Pacific decadal oscillation	1900–2018	https://psl.noaa.gov/data/correlation/pdo.data	Mantua et al. (1997)
5	Solar	Solar flux (10.7 cm)	1948–2018	https://psl.noaa.gov/data/correlation/solar.data	Moen and Brekke (1993)
6	TNA	Tropical Northern Atlantic	1948–2019	https://psl.noaa.gov/data/correlation/tna.data	Enfield et al. (1999)
7	WHWP	Western Hemisphere warm pool	1948–2019	https://psl.noaa.gov/data/correlation/whwp.data	Wang and Enfield (2001)
8	WPI	Western Pacific index	1950–2019	https://psl.noaa.gov/data/correlation/wp.data	Barnston and Livezey (1987)
9	WPSHA	Western Pacific subtropical high area	1951–2019	https://cmdp.ncc-cma.net/Monitoring/cn_stp_wpshp.php?wpsh_elem=wpsh_GM#wpsh	Huang et al. (2018)
10	WPSHI	Western Pacific subtropical high intensity	1951–2019	https://cmdp.ncc-cma.net/Monitoring/cn_stp_wpshp.php?wpsh_elem=wpsh_GM#wpsh	Huang et al. (2018)
11	EASM	East Asian summer monsoon	1948–2018	http://ljp.gcess.cn/dct/page/65577	Li and Zeng (2002)
12	EAWM	East Asian winter monsoon	1948–2018	http://114.215.81.87/	Wang (2014)
13	SAM	Southern Hemisphere annular mode	1948–2017	http://ljp.gcess.cn/dct/page/65609	Nan and Li (2003)
14	SCSSM	South China Sea summer monsoon	1948–2018	http://ljp.gcess.cn/dct/page/65578	Li and Zeng (2003)
15	Niño-3	Niño-3	1948–2020	https://psl.noaa.gov/data/correlation/nina3.data	Rasmusson and Carpenter (1982)
16	Niño-3.4	Niño-3.4	1948–2020	https://psl.noaa.gov/data/correlation/nina34.data	Trenberth (1997)
17	Niño-4	Niño-4	1948–2020	https://psl.noaa.gov/data/correlation/nina4.data	Trenberth and Stepaniak (2001)

breakpoint b_{nb} . In cases when the breakpoint locations are unknown, optimization can be used to find the best set of breakpoint locations that minimizes the overall sum-of-square of the residuals. In the PWLF, we utilize differential evolution for the global optimization (Storn and Price 1997).

3) FORWARD STEPWISE REGRESSION ALGORITHM

To identify the predominant LOACs that influence the NWS changes, a forward stepwise regression algorithm (FSRA) is employed to select the primary CIs. Time periods in most CIs were shorter than ERA-20C (Table 2); thus, the period 1951–2010 was selected to establish the model. The X_i (CIs) and Y (NWS) are selected to establish the regression model, as expressed by Eq. (5):

$$\begin{cases} Y = \alpha_i X_i + \delta, i = 1, 2, \dots, p \\ F^{(1)} = \max\{F_1^{(1)}, F_2^{(1)}, \dots, F_p^{(1)}\}, \\ I = \{X_i | 1 < i < p\} \end{cases} \quad (5)$$

where α_i and δ are the regression coefficients and residual, respectively, $p = 60$ years, $F_i^{(1)}$ is the value of the F test for α_i , and $F^{(1)}$

denotes the maximum value of $F_i^{(1)}$. The X_i is introduced into the model when $F^{(1)} \geq F_{0.01}^{(1)}$, and I_1 denotes the set of those introduced X_i . When X_i is selected, a bivariate regression is estimated between Y and the subsets $\{X_i, X_1\}, \dots, \{X_i, X_{i-1}\}, \{X_i, X_{i+1}\}, \dots, \{X_i, X_p\}$ ($p - 1$ subsets). Similarly, the statistical value of the F test is defined as $F_{X_k}^{(2)}(X_k \neq I_1)$, and the maximum $F_{X_k}^{(2)}$ is selected. If $F_{X_k}^{(2)} \geq F_{0.01}^{(2)}$, X_k is introduced into the model. To avoid overfitting, the above steps are repeated six times, and we validate six CIs that best explain NWS changes (Zeng et al. 2019). Actually, the fit improvement becomes marginal when the number of CIs retrained in the stepwise regression is greater than six. Based on the FSRA, a reconstructed wind speed (RWS) can be obtained, which can be used to estimate the influences of LOACs on NWS (Zeng et al. 2019). To evaluate the importance of the CIs and examine the uncertainty of RWS, we randomly select a 30% subset of the station pools and carry out the FSRA repeated 300 times.

4) OTHER METHODS

A bilinear interpolation method is used to interpolate the grid to measurement stations, and this method has been judged to be least suitable for the transfer of a grid forecast field to another or discrete

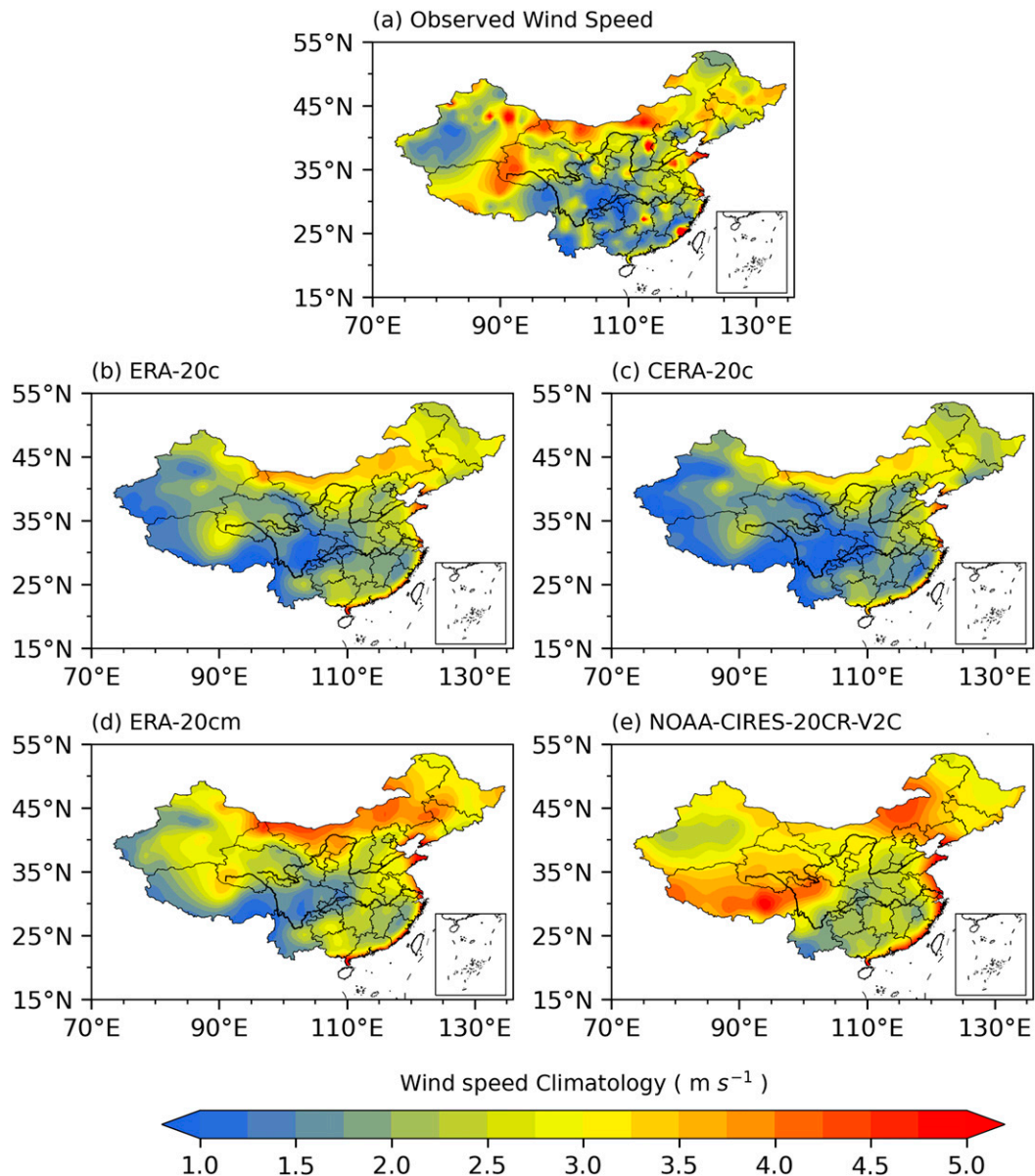


FIG. 1. Spatial patterns of NWSs in (a) observations, (b) ERA-20C, (c) CERA-20C, (d) ERA-20CM, and (e) NOAA-CIRES-20CR-V2C from 1970 to 2010.

observation field (Accadia et al. 2003; Mastilo 2013). The linear trend coefficient is calculated using the least squares method (LSM) and nonparametric Thiel–Sen approach (TSA; Thiel 1950; Sen 1968). A Gaussian low-pass filter with a 9-yr window is used to determine the decadal changes of NWS. The composite analysis is used to discuss the effects of LOACs on the variability of NWS. If the values of normalized CIs are more than 1.0 or less than -1.0 , the corresponding years are deemed as the strong and near-neutral CIs years, respectively. The statistical significance of the trend in NWS is determined using a Student's t test (Azorin-Molina et al. 2014; Minola et al. 2016). To estimate the trends for different wind categories, light, gentle, moderate, and strong winds are defined, as <25 th percentile, >25 th percentile but <50 th percentile, >50 th

percentile but <75 th percentile, and >75 th percentile, respectively. Days with light, gentle, moderate, and strong winds are defined as light, gentle, moderate, and strong windy days, respectively (Wang et al. 2020). The four seasons are defined as winter (December–February), spring (March–May), summer (June–August), and autumn (September–November).

3. Results

a. Evaluating the performance of reanalysis products in simulating the observed NWS

The spatial distributions of NWS in four reanalysis products are similar to that of observations (Fig. 1). Large values of

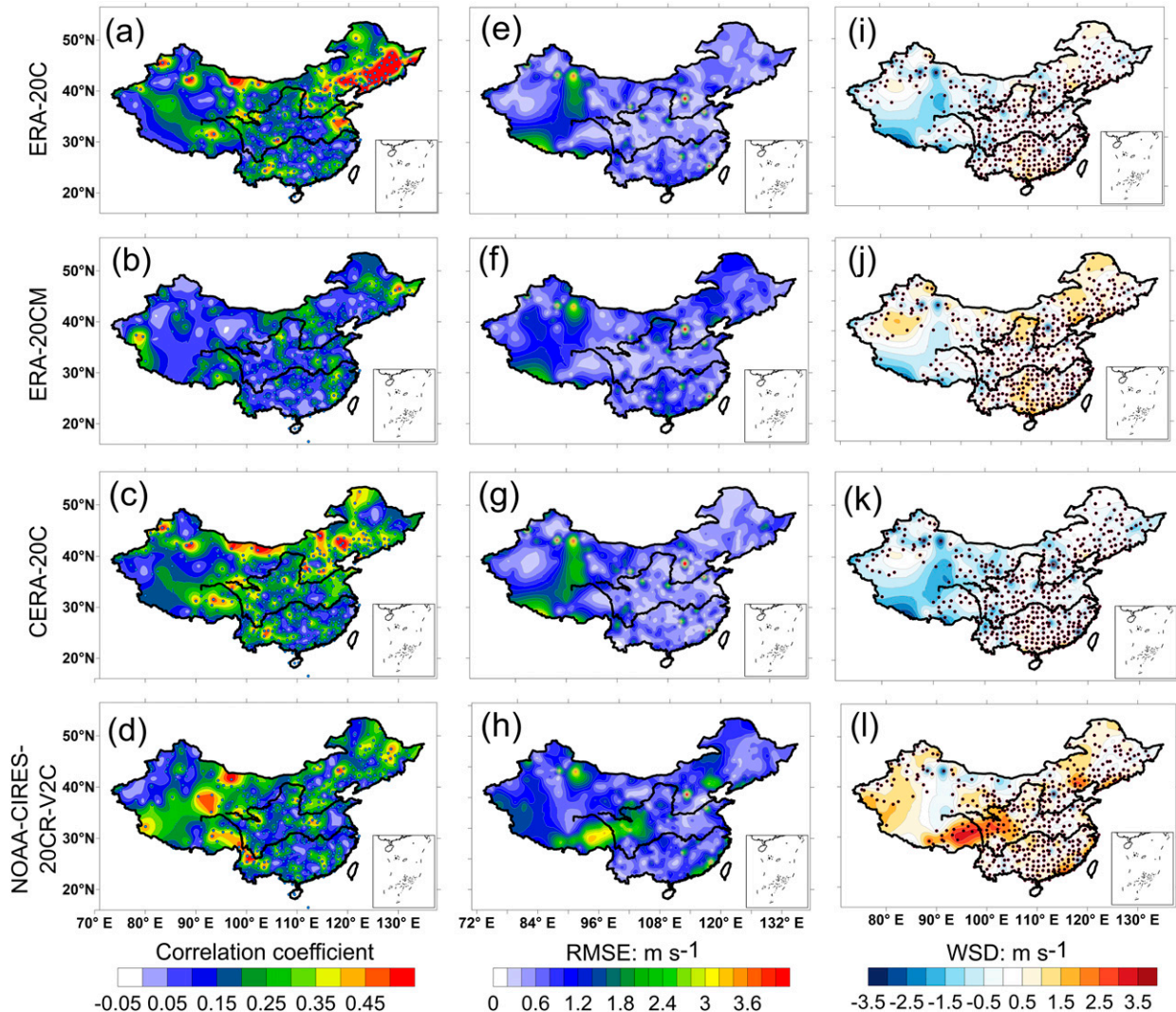


FIG. 2. (a)–(d) Spatial patterns of correlation coefficients, (e)–(h) RMSE, and (i)–(l) WSD between observations and reanalysis datasets between 1970 and 2010. The first, second, third, and fourth rows denote the ERA-20C, ERA-20CM, CERA-20C, and NOAA-CIRES-20CR-V2C, respectively. Dots in (a)–(d) and (i)–(l) denote correlation coefficients and WSDs that pass a t test at the 0.10 level.

NWS are located in Inner Mongolia, northeastern China, Tibetan Plateau (TP) region, and coastal regions. Small values of NWS are located in central China, southwestern China, and southeastern China (Fig. 1a). Three ECMWF reanalysis products are capable of reproducing the spatial patterns of observed NWS; however, NWS found in CERA-20C is smaller than observations (Fig. 1c), and NWS found in ERA-20CM is larger than observations (Fig. 1d). The small value of NWS over the Trim basin in Xinjiang cannot be reproduced in three ECMWF reanalysis products, and the large value of NWS over and around TP cannot be reproduced in CERA-20C (Fig. 1c). NOAA-CIRES-20CR-V2C shows a significantly different pattern compared to the other three ECMWF reanalysis products, especially for the TP, but overestimates NWS across the entirety of China (Fig. 1e).

The correlation coefficient, root-mean-square error (RMSE), and wind speed difference (WSD) between observations and

reanalysis are analyzed (Fig. 2). At an annual scale, reanalysis products and observations mainly show positive correlation over China. The regional mean values of correlation coefficients in ERA-20C (Fig. 2a), ERA-20CM (Fig. 2b), CERA-20C (Fig. 2c), and NOAA-CIRES-20CR-V2C (Fig. 2d) are 0.23, 0.14, 0.23, and 0.20, respectively; 79.0%, 62.0%, 83.0%, and 78.0% of stations display that the correlation coefficients pass the significance t test at the 0.10 level, respectively. The RMSEs between reanalysis and observations show a similar spatial pattern (Figs. 2e–h). The largest RMSE is found in NOAA-CIRES-20CR-V2C (1.08 m s^{-1}) and the smallest RMSE is found in ERA-20C (0.74 m s^{-1}). The WSDs are consistent across reanalysis datasets (Figs. 2i–l). Positive WSD is mainly located in eastern China, and negative WSD is mainly located over and around the TP in three ECMWF reanalysis products (Figs. 2i–k). The WSD in NOAA-CIRES-20CR-V2C mainly display positive values, with the largest positive

TABLE 3. Correlation coefficients, RMSE (m s^{-1}), and WSD (m s^{-1}) between observations and four reanalysis products during all four seasons. The symbols *, **, and *** denote the correlation coefficients that pass a t test at the 90%, 95%, and 99% confidence levels, respectively.

		Winter	Spring	Summer	Autumn
Correlation coefficient	ERA-20C	0.29*	0.32*	0.73***	0.38**
	ERA-20CM	−0.044	0.15	0.08	−0.13
	CERA-20C	0.39**	0.19	0.50***	0.34**
	NOAA-CIRES-20CR-V2C	0.14	0.12	0.48***	0.22
RMSE	ERA-20C	0.20	0.44	0.18	0.16
	ERA-20CM	0.52	0.25	0.33	0.47
	CERA-20C	0.25	0.69	0.46	0.22
	NOAA-CIRES-20CR-V2C	0.91	0.51	0.68	0.70
WSD	ERA-20C	0.07	0.38	0.12	0.03
	ERA-20CM	0.48	0.08	0.27	0.43
	CERA-20C	0.17	0.65	0.44	0.15
	NOAA-CIRES-20CR-V2C	0.89	0.45	0.66	0.68

WSD located in TP (Fig. 2l). At a seasonal scale, all correlations in ERA-20C pass the significance t test at the 0.10 level, and the largest and smallest values are found in summer and winter, respectively (Table 3).

Temporal evolutions of NWS in different datasets are presented in Fig. 3a. The observed NWS shows a significant reduction from 1970 to 2010 ($-0.15 \text{ m s}^{-1} \text{ decade}^{-1}$; $p < 0.01$). Except for ERA-20CM, other three ECMWF reanalysis products show decreasing trends in NWS, with the strongest reduction in ERA-20C ($-0.03 \text{ m s}^{-1} \text{ decade}^{-1}$, $p < 0.10$) and the weakest slowdown in NOAA-CIRES-20CR-V2C ($-0.001 \text{ m s}^{-1} \text{ decade}^{-1}$, $p > 0.10$). ERA-20C assimilates more observational data; however, only observed surface pressure is assimilated in the NOAA-CIRES-20CR-V2C (Table 1). Therefore, the ERA-20C can better reproduce the decreasing trend of observed NWS. A box-and-whisker plot is further employed to evaluate the performance of reanalysis products in simulating NWS across China (Fig. 3b). NOAA-CIRES-20CR-V2C registers the strongest wind episodes, followed by ERA-20C and ERA-20CM, and CERA-20C registers the weakest wind episodes. In this study, we

mainly focus on the climatology and centennial-scale changes of NWS, and as such the fact that interannual variability in ERA-20C is weaker than observation does not affect the research goals. The mean values (medians) in observation, ERA-20C, ERA-20CM, CERA-20C, and NOAA-CIRES-20CR-V2C are 2.40 (2.31), 2.29 (2.29), 2.70 (2.70), 2.03 (2.04), and 3.05 (3.06) m s^{-1} , respectively. Compared to other reanalysis products, the mean and median values of NWS in ERA-20C are closer to observations; meanwhile, the smallest RMSE, and WSD are found in ERA-20C. Consequently, ERA-20C is chosen to investigate the centennial-scale variability of NWS over China.

b. Spatiotemporal characteristics of NWS over China at centennial scale

Temporal evolutions of annual and seasonal mean NWS from 1900 to 2010 are presented in Fig. 4. Annual mean NWS displays a decreasing trend for 1900–25 ($-0.87\% \text{ decade}^{-1}$) and 1957–2010 ($11.75\% \text{ decade}^{-1}$) and an increasing trend for 1926–56 ($55.47\% \text{ decade}^{-1}$). Such decadal variations in NWS are also found in the other three reanalysis products (Fig. S2).

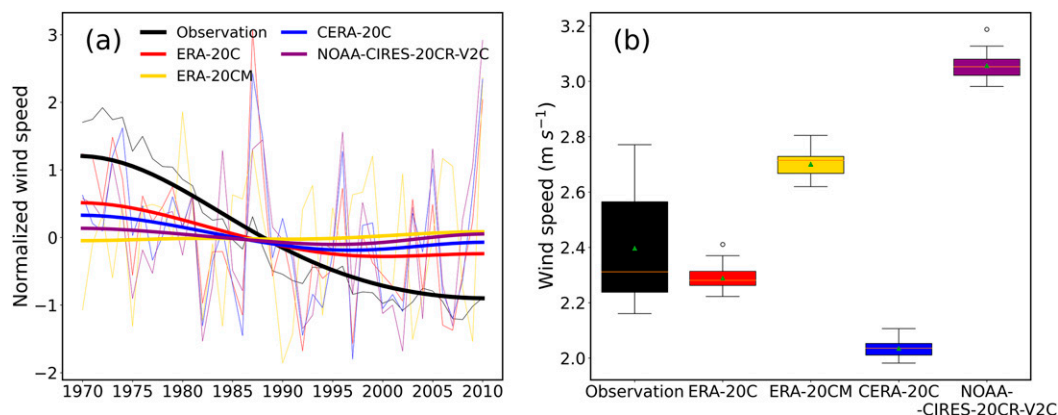


FIG. 3. (a) Temporal evolutions in NWSs in observations and reanalysis products from 1970 to 2010. (b) Box-and-whisker plot of NWSs. The thick lines in (a) denote the Gaussian low-pass filter with a 9-yr window. The mean (central triangle), median (middle lines), 25th and 75th percentile range (boxes), maximum and minimum values (upper and lower horizontal lines), and mild outliers (circles) are presented in a box-and-whisker plot.

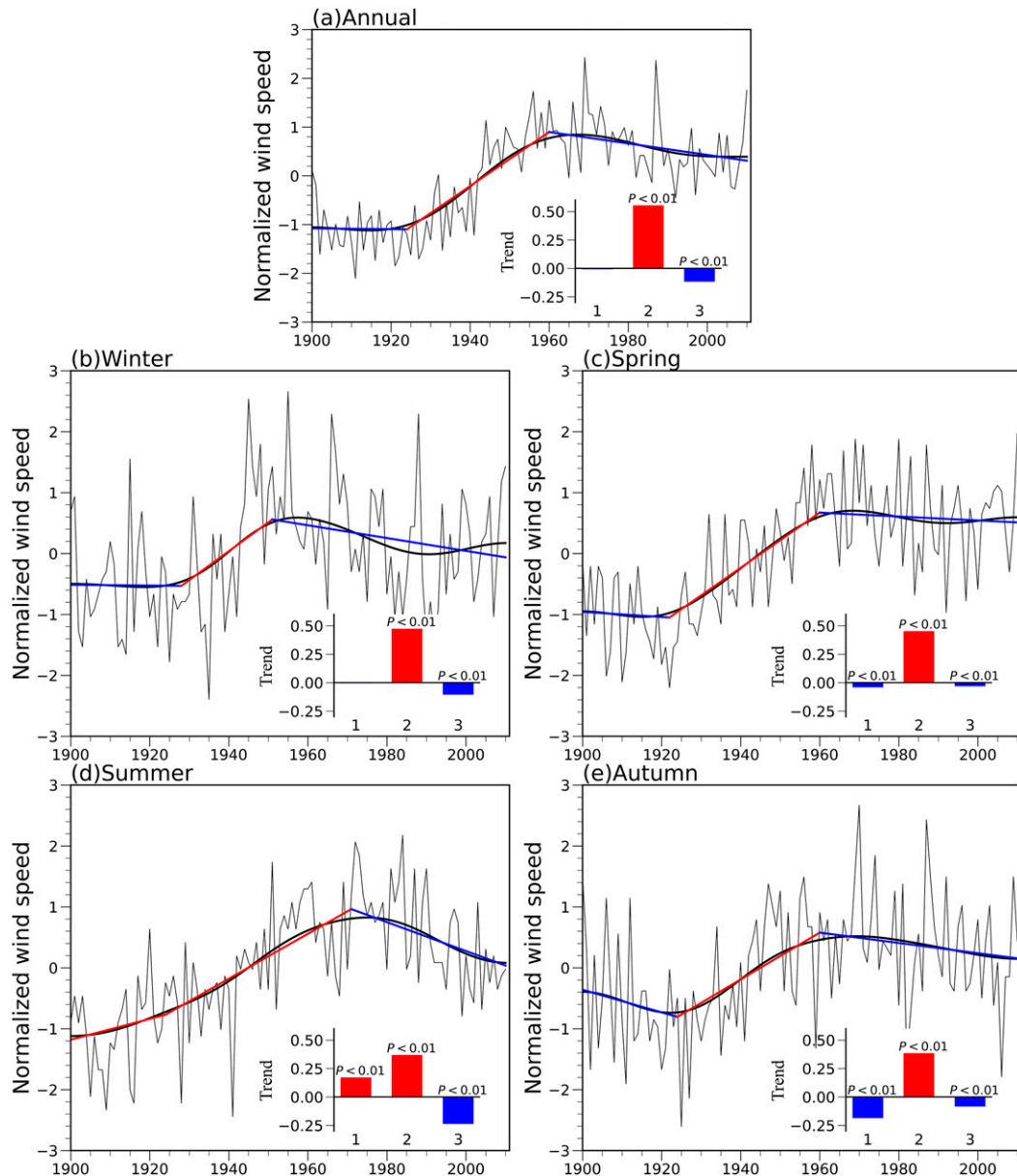


FIG. 4. Temporal evolutions of (a) annual mean and (b) winter, (c) spring, (d) summer, and (e) autumn NWSs during the period from 1900 to 2010. Red and blue lines denote piecewise linear function fit curves during different periods. Thick black lines denote the 9-yr Gaussian low-pass filter. The trends during three periods are presented using the inset axis. In the inset, $P < 0.01$ denotes significant trends at the 0.01 level.

Seasonal NWS from 1900 to 1925 also experienced downward trends except for summer. The most significant decrease is found in autumn (-18.55% decade $^{-1}$) (Fig. 4e). From 1926 to 1956, NWS shows an increasing trend during all four seasons, with the strongest increase in winter (47.35% decade $^{-1}$) and weakest increase in summer (36.88% decade $^{-1}$). From 1957 to 2010, NWS experiences downward trends in all four seasons, with the most significant decrease in summer (-23.73% decade $^{-1}$). The significance levels of all trends are shown in the inset of Fig. 4. To determine the significance of trend coefficients calculated by LSM, the TSA is also used to compute the slopes of NWSs. The

trends calculated based on LSM are consistent with those computed based on TSA. The annual and seasonal mean NWSs show significant decadal changes at the centennial scale, which is also revealed by a 9-yr Gaussian low-pass filter.

Spatial patterns of mean, variance, and trends of NWS at the centennial scale are shown in Fig. 5. The mean values of NWS show similar spatial pattern during the three periods of interest (Figs. 5a–c). Large variances are found over TP and Inner Mongolia and small variances are found over central China and Xinjiang (Figs. 5d–f). Hence, significant changes in climatology of NWS at centennial scale do not occur. However, a significant

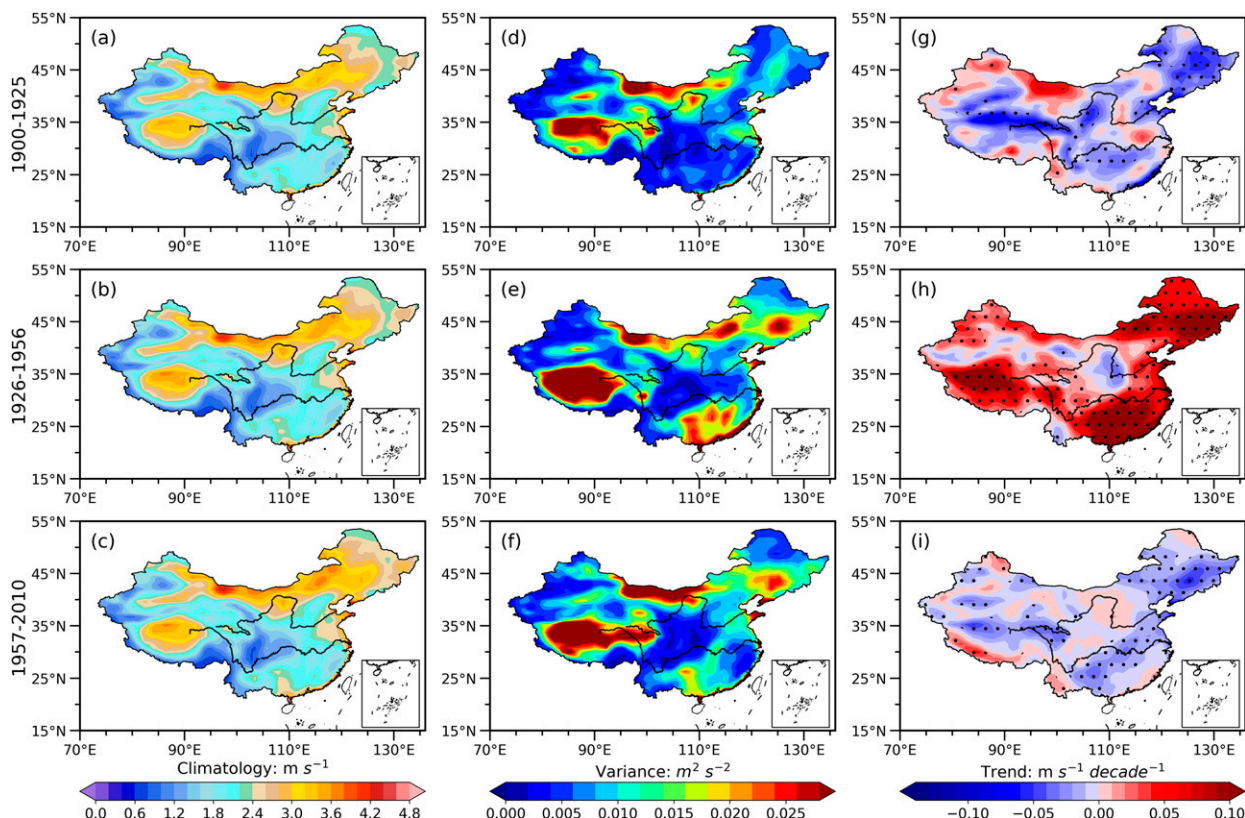


FIG. 5. (a)–(c) Spatial patterns of mean values of NWSs (m s^{-1}), (d)–(f) variances of NWSs ($\text{m}^2 \text{s}^{-2}$), and (g)–(i) the linear trends of NWSs ($\text{m s}^{-1} \text{decade}^{-1}$) during the periods 1900–25 [in (a), (d), and (g)], 1926–56 [in (b), (e), and (h)], and 1957–2010 [in (c), (f), and (i)]. Black dots in (g), (h), and (i) denote significant trend coefficients at the 0.10 level.

difference is found in the trend of NWS (Figs. 5g–i). NWS mainly displays decreasing trends from 1900 to 1925 and from 1957 to 2010, and an increasing trend from 1926 to 1956. The significant decreases are found in northeastern China, and significant increases in northern China, southeastern China, and TP. During the periods 1900–25 and 1957–2010, 69.73% and 69.47% of total grid cells experience downward trends, respectively, with 13.35% and 22.45% of these grid cells passing a significance t test at the 0.10 level. From 1926 to 1956, 84.95% of grid cells show upward trends, and 60.32% of these are significant at the 0.10 level.

c. Variability in different windy days and wind categories at centennial scale

Given that the decadal changes of NWS at centennial scale could cause the changes in different windy days, the frequency trends for different categories of windy days are revealed (Fig. 6). The reductions in annual mean NWS from 1900 to 1925 and from 1957 to 2010 are due to the decreases in strong windy days, with trends of -6.64 and -4.66 days decade^{-1} , respectively (Fig. 6a). The upward trend in annual mean NWS from 1926 to 1956 is also due to increases in strong windy days (23.55 days decade^{-1}). At a seasonal scale, from 1926 to 1956, the increasing trends in NWS in all seasons aligns with the increases in strong windy days, and that all trends pass the

significance t test at the 0.001 level. The increased winter NWS is a result of increases in strong and moderate windy days for 1926–56, with trend coefficients of 0.43 and 5.43 days decade^{-1} , respectively (Fig. 6b). The decreased spring and autumn NWSs during 1900–25 and 1957–2010 are concurrent with the decreases in days with strong winds (Figs. 6c,e). The increase in summer NWS from 1926 to 1956 is a result of the increase in strong windy days (Fig. 6d). Additionally, the trends for light, gentle, moderate, and strong winds during three periods are analyzed (Fig. S3). At an annual scale, each wind category shows an upward trend from 1926 to 1956 and downward trends from 1900 to 1925 and from 1957 to 2010 (Fig. S3a). The seasonal differences in different categories of winds are considerable. All winds strengths display increasing trends from 1926 to 1956 (Figs. S3b–e). From 1900 to 1925 and from 1957 to 2010, all wind categories show decreasing trends except in winter. In spring, all wind categories show more substantial decreasing trends from 1957 to 2010 than from 1900 to 1925 (Fig. S3c).

4. Causes of NWS trend changes

Wind is generated by the pressure-gradient force associated with uneven heating of Earth's surface, and the heterogeneity is to a large extent described by CIs for oscillations (Zeng et al.

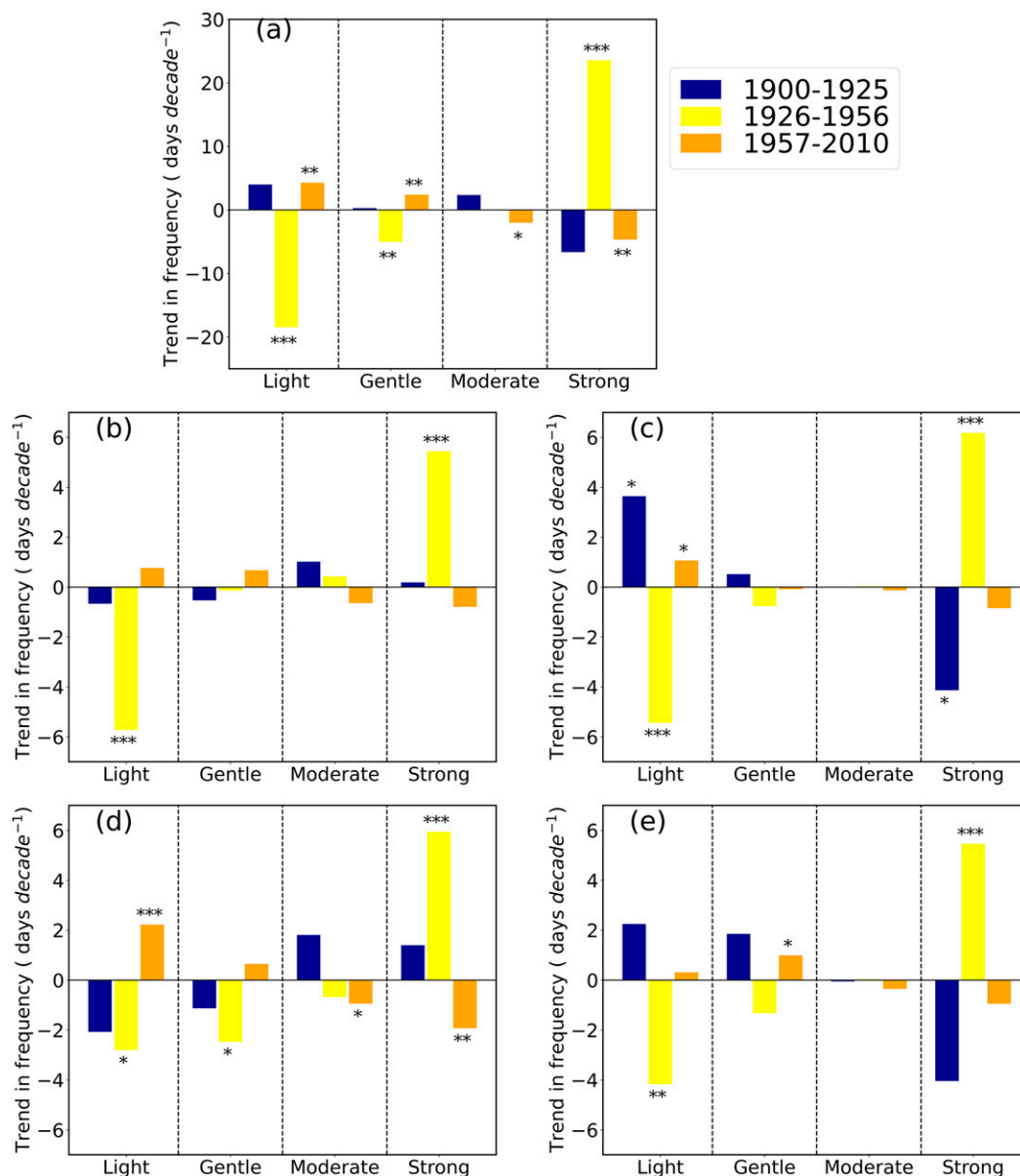


FIG. 6. Linear trends in annual (a) and seasonal (b)–(e) frequencies of different categories of winds (day-decade⁻¹) during the periods 1900–25, 1926–56, and 1957–2010, respectively. The symbols *, **, *** denote significant trends at the 0.10, 0.01, and 0.001 levels, respectively.

2019). Most studies have shown that variations in LOACs can cause adjustments in global circulation, generate stationary atmospheric waves, and induce massive reorganizations of wind patterns (Naizghi and Ouarda 2017; Nchaba et al. 2017; Zeng et al. 2019). Hence, we investigate the relationships between the NWS and LOACs. Based on FSRA, the selected six CIs are shown in Table 4. At an annual scale, the Arctic Oscillation (AO), Niño-3, western Pacific (WP), NAO, PDO, and East Asian summer monsoon (EASM) are selected. The total explanatory power for the six CIs is 66%. At a seasonal scale, variations in NWS are controlled by different LOACs.

During winter, spring, summer, and autumn, the total explanatory powers for the six CIs are 74%, 71%, 46%, and 55%, respectively. The quantified relationship between NWS and LOACs implies that the decadal changes in NWS could be highly influenced by changes in LOACs.

Based on the selected CIs, an RWS can be obtained (Fig. 7). Uncertainties are reflected in the interquartile range of the results based on a randomly selected 30% subset of the stations in China repeated 300 times. The annual and seasonal mean RWSs match well with the original wind speeds from 1951 to 2010. The RWSs are capable of reproducing the temporal

TABLE 4. The selected six CIs based on a forward stepwise regression algorithm during the period from 1951 to 2010. Rank denotes the order in which CIs entered the model. The earlier a CI enters the model, the larger its explanatory power. The numbers in parentheses denote the selected numbers in the test repeated 300 times. Total explanation refers to total variation explained by the model at the annual and seasonal scales.

Rank	Annual	Winter	Spring	Summer	Autumn
1	AO (300)	NAO (291)	AO (300)	Niño-3 (288)	Niño-3 (268)
2	Niño-3 (295)	EAWM (297)	EAWM (296)	AO (299)	SAMI (300)
3	WP (299)	AMM (257)	PDO (300)	SAMI (299)	EAWM (294)
4	NAO (300)	AO (230)	TNA (300)	EAWM (268)	Solar (156)
5	PDO (153)	WPSHI (205)	NAO (171)	AMM (84)	WPSHA (280)
6	EASM (135)	WP (129)	WPSHA (119)	PDO (132)	SCSM (105)
Total explanation	66%	74%	71%	46%	55%

changes in original wind speeds, with the explained power exceeding 66%. The largest explanation is found in winter (74%) and the smallest in summer (46%). These results mean that the effects of LOACs on NWS over China are significant. Because CIs at the centennial scale are not available, based on

the correlations between RWSs and original wind speeds, we infer that the changes in annual mean NWS over China at the centennial scale could be highly influenced by AO, ENSO, WP, NAO, PDO, and EASM. Similar results have also been reported in the previous studies (Xu et al. 2006; Lin et al. 2013;

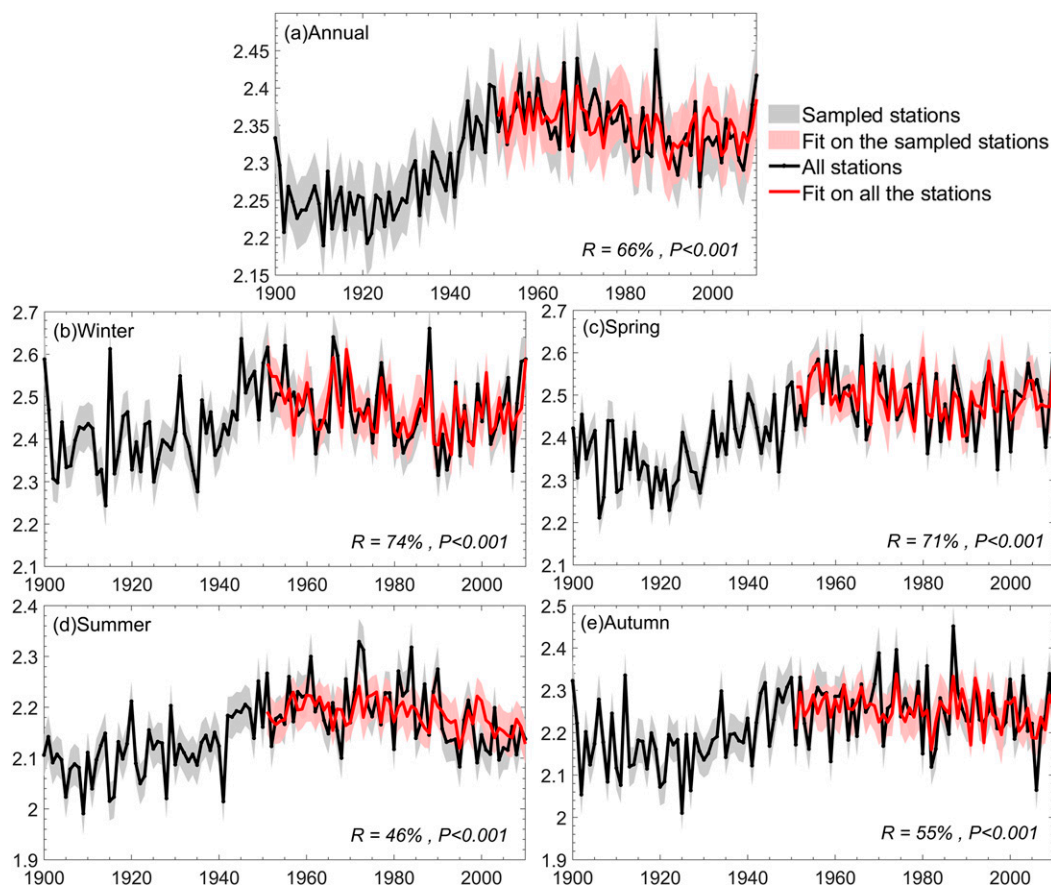


FIG. 7. Temporal evolutions of ERA-20C wind speed (black lines) and RWS (red lines) based on a forward stepwise regression algorithm. Uncertainties are represented by the interquartile range of the results based on a randomly selected 30% subset of the station pools in China (repeated 300 times). Inset numbers are the correlation coefficients and their significance between ERA-20C and RWD. (a) Annual mean, (b) winter, (c) spring, (d) summer, and (e) autumn.

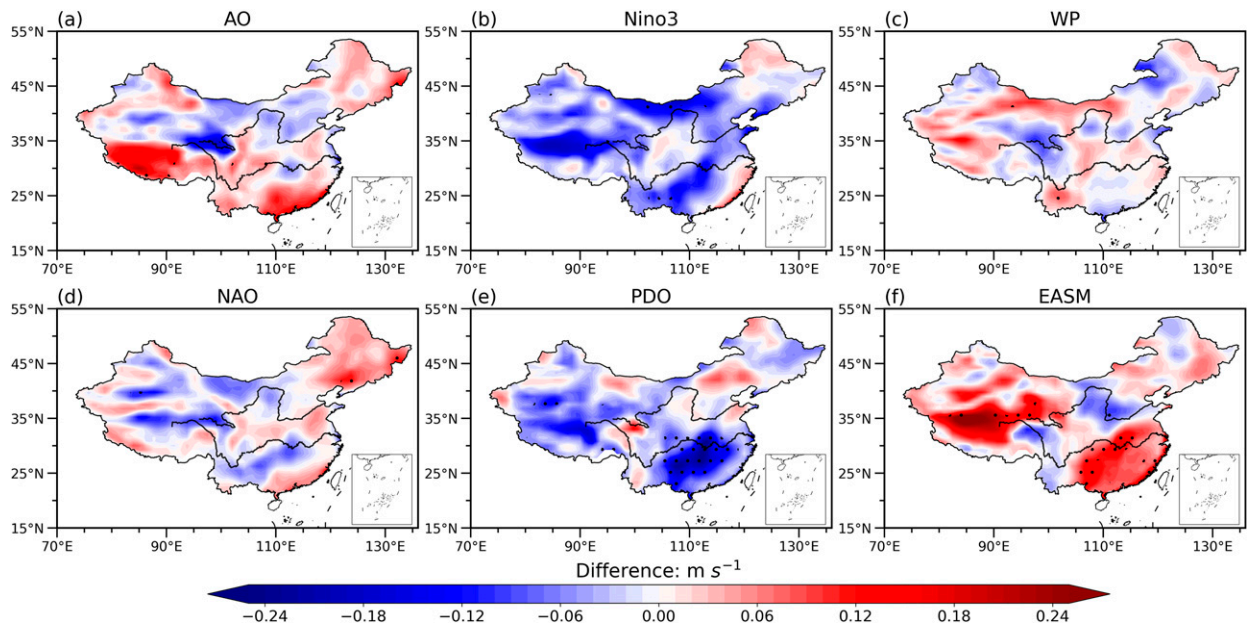


FIG. 8. Spatial patterns of WSD between strong CIs years and weak CIs years during the period from 1951 to 2010. Black dots denote the wind speed differences that pass a t test at the 0.01 confidence level.

Wu et al. 2018b; Zhang et al. 2020). No single CI has a large explanatory power for NWS changes, but when taken as a whole they do generate a large amount of explanatory power (Zeng et al. 2019). Accordingly, we conclude that NWS changes cannot be simply linked to just one ocean–atmosphere oscillation, but rather should be determined by the combined effects of variations in various LOACs.

We further construct the composite annual mean WSD for the years that displayed strong and weak CIs (Fig. 8). To facilitate interpretation, the positive and negative WSDs between strong and near-neutral CIs years are defined as +WSDs and –WSDs, respectively. The spatial patterns of WSDs are different with different CIs. The +WSDs and –WSDs among strong and weak AO years are mainly located in southern and northern China, respectively. Here, 61.0% and 39.0% of total grid cells show +WSDs and –WSDs in strong and weak AO years, respectively (Fig. 8a). The WSD mainly shows negative values in most regions of China in the strong El Niño years, as the grid cells that show –WSDs account for 77.7% of the total (Fig. 8b). Compared to other CIs, the effects of WP and NAO on the NWS changes are relatively small; meanwhile, the spatial patterns of WSD are inhomogeneous (Figs. 8c,d). The WSDs between strong and weak PDO years show negative values across China; the large –WSDs are located in southeastern China, which reach -0.2 m s^{-1} (Fig. 8e). The effects of EASM on NWS are mainly concentrated in southeastern China and TP (Fig. 8f). Compared to Fig. 8e, a reversed spatial pattern of WSDs is presented in Fig. 8f. Consequently, the effects of LOACs on NWS changes over China exhibit regional differences. We can acquire the predominant LOACs that cause the NWS changes from the FSRA; nevertheless, we cannot exclude other CIs that may aid in forcing the NWS changes.

5. Discussion

a. Possible mechanisms of LOACs affect NWS changes over China

We have shown that the decadal changes of NWS are mainly determined by the combined effects of LOACs. The changes of seasonal NWS are controlled by different LOACs (Table 4), so it is difficult to reveal the processes whereby each ocean–atmosphere oscillation influences seasonal NWS. In this subsection, we discuss the processes of the dominant LOACs (viz., AO, ENSO, WP, NAO, PDO, and EASM) that affect annual mean NWS. These CIs have been considered as the primary LOACs that induce NWS changes over China (Xu et al. 2006; Lin et al. 2013; Wu et al. 2018a; Zhang et al. 2020), which indirectly demonstrate the performance of the FSRA in its selection of LOACs. There are some theories for the processes that govern changes in these CIs that affect NWS.

With respect to AO, during the positive AO phase, the Northern Hemisphere is characterized by a decrease in surface pressure difference between high-latitudes and midlatitudes; meanwhile, the Ferrel cell at high latitudes strengthens, which induces a meridional flow anomaly (Thompson and Wallace 1998; Li and Wang 2003). The anomalous meridional flow transports heat from lower latitudes to higher latitudes, thereby reducing the north–south temperature gradient, which in turn decreases NWS. ENSO is a result of sea–air interaction on multiple space–time scales, which has a significant effect on the Asian monsoon circulation (Ni et al. 1995). During a strong El Niño year, the location of western Pacific subtropical high moves northward and the Tibetan high weakens, especially in summer. The effects of ENSO on the East Asian atmospheric circulations are significant (Lu et al. 2016). Therefore, the Niño index can be best

utilized when entering the model in summer (Table 4). Some studies have shown an ENSO–EASM relationship (Huang et al. 2018). Accordingly, ENSO effects on NWS could be a result of its relationship to the EASM changes. As for WP, Zhang et al. (2020) proposed that negative phases of WP were associated with below-average air temperatures over the lower latitudes of the northwestern Pacific during summer, which reflects the enhanced land–sea temperature gradient and pronounced zonal and meridional variations in the location and intensity of the East Asian jet stream. Furthermore, the negative phases of WP facilitate the movement of tropical cyclones into mainland China, and tropical cyclones induce more strong winds (Zhang et al. 2020). During strong NAO episodes, both the Siberian cold high and East Asian trough are weaker than during a weak NAO, which induces a weak East Asian winter monsoon. Hence, the north–south pressure gradient decreases in East Asia. The pressure gradient force is the driving force of NWS, so the NWS decreases during a strong NAO. The effects of NAO on NWS could be more significant during winter than other seasons (Li 2005); therefore, the NAO preferentially enter the model in winter (Table 4). As for PDO, the temperature gradients during the negative and positive phases of PDO generate the easterly and westerly components of NWS, which decrease and increase the prevailing westerly winds in the midlatitudes, respectively (Zhang et al. 2018; Zeng et al. 2019). In regard to EASM, strong and weak EASM are associated with increases and decreases in the surface air temperature (SAT) difference between the land and sea, respectively. Changes in the SAT difference between land and sea caused by EASM influence the NWS changes (Ding 1994; Wang et al. 2001; Lu et al. 2016; Huang et al. 2018). The effects of EASM on NWS are more significant over southeastern China and TP (Xu et al. 2006); hence, the larger WSDs between strong and weak EASM years are found in these regions (Fig. 8f).

The interaction and modulation among different LOACs are considerable, so it is difficult to isolate and quantify the contribution of different LOACs to NWS changes and reveal the mechanisms whereby the LOACs affect NWS. Furthermore, the CIs may not be independent, and we cannot guarantee that the predictand and predictors satisfy a linear relationship. Investigating whether a nonlinear relationship between NWS and CIs can better express the effects of LOACs on NWS should be performed in the future.

b. Possible causes of reanalysis products underestimate the terrestrial stilling

Four centennial-scale reanalysis products generated at centers with advanced assimilation systems are able to capture the climatology of NWS. However, all reanalysis products underestimate the decreasing trend in NWS, which may be due to the following reasons.

Different assimilation data types could be a primary cause of inconsistencies between the four centennial-scale reanalysis products. For example, the NOAA-CIRES-20CR-V2C assimilates only surface pressure; however, the ERA-20C assimilates surface pressure, sea level pressure, and surface marine wind, and the CERA-20C assimilates surface pressure, surface marine wind, and ocean temperature. Therefore, ERA-20C and CERA-20C can better capture the decreasing trends in NWS, and

reanalysis product that only assimilate surface pressure data are not able to fully represent NWS changes. That the assimilation of sea level pressure and surface wind is important to improve the performance of reanalysis products in simulating the trends of NWS speaks to the potential of further improvements with the addition of more observed variables (Hersbach et al. 2015).

The performance of reanalysis products in simulating the trends of NWS could be also influenced by models simulating sea surface temperature (SST). Zeng et al. (2019) found that in the regions where the Atmospheric Model Intercomparison Project (AMIP) model (atmospheric simulations forced with observed SST) capture the stilling, the reanalysis products are also capable of reproducing the stilling. In contrast, for regions where AMIP simulations do not capture the stilling, the reanalysis products fail to reproduce the stilling. ERA-20C has been extensively used for assessing the long-term trends and variability of NWS (Bett et al. 2017; Jung et al. 2018, 2019; Foley 2019), and has demonstrated capability to capture the changes of some LOACs, such as Niño-3, Southern Oscillation, NAO, Pacific–North American, and so forth (Poli et al. 2016). Consequently, a reanalysis that can simulate the SST and LOACs could better capture the NWS changes.

Scale differences and challenges with topography in models could also influence performance of reanalysis products in capturing NWS trends (Zeng et al. 2019; Fan et al. 2021). Our results show that the magnitude of NWS in ERA-20C is closest to observations, which may be due to the relatively high spatial resolution of ERA-20C. NWS changes are also sensitive to changes in surface roughness and topography (Vautard et al. 2010; Guo et al. 2017). In the gridded reanalysis products, each gridcell value represents the mean wind speed over that area. These estimates will show considerably less variability in NWS compared to that of the observing station, especially for the regions with complex terrain and when NWS has large spatio-temporal gradients, the gridded spatial variability of NWS will be smaller (Fan et al. 2021). Consequently, with higher resolution in reanalysis products, more topographical information can be included and thereby better capture NWS changes.

Multidecadal measurements are scarce in some regions, which makes it difficult to carry out large-scale studies on NWS changes at the centennial scale. Therefore, global reanalysis products represent a potential tool for assessing the NWS changes. The models do well at simulating climate dynamics but neglect changes in surface roughness (Kalnay and Cai 2003; Lim et al. 2005; Vautard et al. 2010), so the spatiotemporal characteristics in NWS at the centennial scale could be mainly caused by LOACs, and any signal from changes in surface roughness should not be substantial. In the future, to improve the performance of reanalysis products in simulating the NWS changes, more efforts are required to improve surface process parameterization schemes and their connections to ocean–atmosphere circulations in climate models and operational weather data assimilation systems (Zeng et al. 2019).

c. Other causes for changes in NWS over China

The characteristics of centennial-scale NWS over China have not been reported in the previous studies, so investigating NWS on these long time scales may provide new insights or at

least a perspective on the important shifts in NWS over many decades. Actually, besides the LOACs, NWS reductions in China could also be induced by other factors. For instance, urbanization is likely a contributor to the reduction in NWS over the past several decades (Vautard et al. 2010; Zha et al. 2016, 2021; Wu et al. 2018c; Zhang et al. 2019). Greenhouse gas emissions could alter the thermodynamic and dynamic processes of the atmosphere and induce NWS changes (Chen et al. 2012; Zhang et al. 2017). Anthropogenic aerosols can strengthen the atmospheric stability due to aerosol interactions with radiation, thereby slowing NWS (Bichet et al. 2012; Li et al. 2016). Anthropogenic heat release enhances vertical mixing and could lead to increases in NWS, especially in some megacity clusters (Zhang et al. 2015). The effects of the aforementioned factors on variations of NWS are not isolated and quantified in the current study but warrant future investigation. Nevertheless, the results presented here are an important step toward improving understanding of NWS trends in China and beyond.

6. Conclusions

In this study, the spatiotemporal characteristics of NWS changes over China at the centennial scale and potential causes are revealed; meanwhile, the performance of four reanalysis products in simulating climatology and trends in NWS over China is evaluated. The key results are now summarized.

ERA-20C is capable of reproducing the climatology and decreasing trend of observed annual mean NWS from 1970 to 2010. The regional mean correlation coefficient, RMSE and WSD between ERA-20C and observations are 0.23, 0.74, and -0.031 m s^{-1} , respectively. Seasonally, all temporal correlations between ERA-20C and observations pass a significance t test at the 0.10 level, and the largest and smallest values are found in summer and winter, respectively. Compared to other centennial-scale reanalysis products, the ERA-20C can better simulate the climatology and long-term changes of NWS over China.

Temporal evolutions of annual mean NWS over China from 1900 to 2010 experience three phases. Between the periods of 1900–25 and 1957–2010, the annual mean NWS displays a decreasing trend, and the decreasing trends are caused by the decreases in the frequency of strong windy days. From 1926 to 1956, the annual mean NWS shows an increasing trend, attributed to an increase in the frequencies of moderate and strong windy days. Similar to the annual mean NWS, the seasonal NWSs at the centennial scale also experience three phases.

The decadal changes in NWS over China at the centennial scale are influenced by the combined effects of changes in various LOACs. The RWS obtained based on LOACs matches well with the original wind speed from 1951 to 2010. The variability in annual mean NWS could be influenced by AO, ENSO, WP, NAO, PDO, and EASM, with a total variance explained by the six CIs of 66%. The seasonal variations in NWS are controlled by different LOACs. During winter, spring, summer, and autumn, the total explanations for the dominant LOACs are 74%, 71%, 46%, and 55%, respectively.

Acknowledgments. We cordially thank the reviewers for their thorough comments and constructive suggestions, which

improved this study significantly. We also thank all the dataset providers. The work is supported by National Key Research and Development Program of China (2016YFA0600403, 2018YFA06006004), National Natural Science Foundation of China (42005023, 41775087, 41875178), project funded by China Postdoctoral Science Foundation (2019M660761), Natural Science Foundation of Shanghai (18ZR1410700), and Nanjing Meteorological Bureau Scientific Project (NJ202103). This work is also supported by the Special Research Assistant Project of Chinese Academy of Sciences, the Program for Key Laboratory in University of Yunnan Province, and the Chinese Jiangsu Collaborative Innovation Center for Climate Change.

REFERENCES

- Accadia, C., S. Mariani, M. Casaioli, A. Lavagnini, and A. Speranza, 2003: Sensitivity of precipitation forecast skill scores to bilinear interpolation and a simple nearest-neighbor average on high-resolution verification grids. *Wea. Forecasting*, **18**, 918–932, [https://doi.org/10.1175/1520-0434\(2003\)018<0918:SOPFSS>2.0.CO;2](https://doi.org/10.1175/1520-0434(2003)018<0918:SOPFSS>2.0.CO;2).
- Alexandersson, H., 1986: A homogeneity test applied precipitation data. *Int. J. Climatol.*, **6**, 661–675, <https://doi.org/10.1002/joc.3370060607>.
- Azarin-Molina, C., and Coauthors, 2014: Homogenization and assessment of observed near-surface wind speed trends over Spain and Portugal, 1961–2011. *J. Climate*, **27**, 3692–3712, <https://doi.org/10.1175/JCLI-D-13-00652.1>.
- , J. A. Guijarro, T. R. McVicar, S. M. Vicente-Serrano, D. L. Chen, S. Jerez, and F. Espirito-Santo, 2016: Trends of daily peak wind gusts in Spain and Portugal, 1961–2014. *J. Geophys. Res. Atmos.*, **121**, 1059–1078, <https://doi.org/10.1002/2015JD024485>.
- , S. Rehman, J. A. Guijarro, T. R. McVicar, L. Minola, D. Chen, and S. M. Vicente-Serrano, 2018: Recent trends in wind speed across Saudi Arabia, 1978–2013: A break in the stilling. *Int. J. Climatol.*, **38**, e966–e984, <https://doi.org/10.1002/joc.5423>.
- Barnston, A. G., and R. E. Livezey, 1987: Classification, seasonality and persistence of low-frequency atmospheric circulation patterns. *Mon. Wea. Rev.*, **115**, 1083–1126, [https://doi.org/10.1175/1520-0493\(1987\)115<1083:CSAPOL>2.0.CO;2](https://doi.org/10.1175/1520-0493(1987)115<1083:CSAPOL>2.0.CO;2).
- Berrisford, P., I. Tobin, R. J. H. Dunn, R. Vautard, and T. R. McVicar, 2015: Land surface wind speed [in “State of the Climate in 2014”]. *Bull. Amer. Meteor. Soc.*, **96** (7), S33–S34, <https://doi.org/10.1175/2015BAMSStateoftheClimate.1>.
- Bett, P. E., H. E. Thornton, and R. T. Clark, 2017: Using the twentieth century reanalysis to assess climate variability for the European wind industry. *Theor. Appl. Climatol.*, **127**, 61–80, <https://doi.org/10.1007/s00704-015-1591-y>.
- Bichet, A., W. Wild, D. Folini, and S. Schar, 2012: Causes for decadal variations of speed over land: Sensitivity studies with a global climate model. *Geophys. Res. Lett.*, **39**, L11701, <https://doi.org/10.1029/2012GL051685>.
- Brazdil, R., K. Chroma, P. Dobrovolny, and R. Tolasz, 2009: Climate fluctuations in the Czech Republic during the period 1961–2005. *Int. J. Climatol.*, **29**, 223–242, <https://doi.org/10.1002/joc.1718>.
- Chen, G. X., T. Iwasaki, H. L. Qin, and W. M. Sha, 2014: Evaluation of the warm-season diurnal variability over East Asia in recent reanalyses JRA-55, ERA-Interim, NCEP

- CFSR, and NASA MERRA. *J. Climate*, **27**, 5517–5537, <https://doi.org/10.1175/JCLI-D-14-00005.1>.
- Chen, L., S. C. Pryor, and D. L. Li, 2012: Assessing the performance of Intergovernmental Panel on Climate Change AR5 climate models in simulating and projecting wind speeds over China. *J. Geophys. Res.*, **117**, D24102, <https://doi.org/10.1029/2012JD017533>.
- , D. Li, and S. C. Pryor, 2013: Wind speed trends over China: Quantifying the magnitude and assessing causality. *Int. J. Climatol.*, **33**, 2579–2590, <https://doi.org/10.1002/joc.3613>.
- Chiang, J. C. H., and D. J. Vimont, 2004: Analogous Pacific and Atlantic meridional modes of tropical atmosphere–ocean variability. *J. Climate*, **17**, 4143–4158, <https://doi.org/10.1175/JCLI4953.1>.
- China Meteorological Administration, 2003: *Ground Surface Meteorological Observation*. China Meteorological Press, 157 pp.
- Compo, G. P., J. S. Whitaker, and P. D. Sardeshmukh, 2006: Feasibility of a 100-year reanalysis using only surface pressure data. *Bull. Amer. Meteor. Soc.*, **87**, 175–190, <https://doi.org/10.1175/BAMS-87-2-175>.
- , and Coauthors, 2011: The Twentieth Century Reanalysis Project. *Quart. J. Roy. Meteor. Soc.*, **137** (654), 1–28, <https://doi.org/10.1002/qj.776>.
- Dadaser-Celik, F., and E. Cengiz, 2014: Wind speed trends over Turkey from 1975–2006. *Int. J. Climatol.*, **34**, 1913–1927, <https://doi.org/10.1002/joc.3810>.
- Ding, Y. H., 1994: The summer monsoon in East Asia. *Monsoons over China*, Kluwer Academic, 1–90.
- Earl, N., S. Dorling, R. Hewston, and R. Von Glasow, 2013: 1980–2010 variability in U.K. surface wind climate. *J. Climate*, **26**, 1172–1191, <https://doi.org/10.1175/JCLI-D-12-00026.1>.
- Enfield, D. B., A. M. Mestas-Nunez, D. A. Mayer, and L. Cid-Serrano, 1999: How ubiquitous is the dipole relationship in tropical Atlantic sea surface temperature? *J. Geophys. Res.*, **104**, 7841–7848, <https://doi.org/10.1029/1998JC900109>.
- Fan, W. X., Y. Liu, A. Chappell, L. Dong, R. Xu, M. Ekstrom, T.-M. Fu, and Z. Zeng, 2021: Evaluation of global reanalysis land surface wind speed trends to support wind energy development using in situ observations. *J. Appl. Meteor. Climatol.*, **60**, 33–50, <https://doi.org/10.1175/JAMC-D-20-0037.1>.
- Foley, A. M., 2019: Long-term trends in large-scale circulation behaviour and wind storms for North Atlantic islands: A multi-data analysis using ERA-20C and meteorological station data. *Climatic Change*, **155**, 323–338, <https://doi.org/10.1007/s10584-019-02467-w>.
- Fu, G. B., J. J. Yu, Y. C. Zhang, S. S. Hu, R. L. Quyang, and W. B. Liu, 2011: Temporal variation of wind speed in China for 1961–2007. *Theor. Appl. Climatol.*, **104**, 313–324, <https://doi.org/10.1007/s00704-010-0348-x>.
- Fyllas, N. M., and Coauthors, 2009: Basin-wide variations in foliar properties of Amazonian forest: Phylogeny, soils and climate. *Biogeosciences*, **6**, 2677–2708, <https://doi.org/10.5194/bg-6-2677-2009>.
- Giese, B. S., H. F. Seidel, G. P. Compo, and P. D. Sardeshmukh, 2016: An ensemble of ocean reanalyses for 1815–2013 with sparse observational input. *J. Geophys. Res. Oceans*, **121**, 6891–6910, <https://doi.org/10.1002/2016JC012079>.
- Gilliland, J. M., and B. D. Keim, 2018: Surface wind speed: Trend and climatology of Brazil from 1980–2014. *Int. J. Climatol.*, **38**, 1060–1073, <https://doi.org/10.1002/joc.5237>.
- Greene, J. S., M. Chatelain, M. Morrissey, and S. Stadler, 2012: Estimated changes in wind speed and wind power density over the western high plains, 1971–2000. *Theor. Appl. Climatol.*, **109**, 507–518, <https://doi.org/10.1007/s00704-012-0596-z>.
- Guo, H., M. Xu, and Q. Hu, 2011: Changes in near-surface wind speed in China: 1969–2005. *Int. J. Climatol.*, **31**, 349–358, <https://doi.org/10.1002/joc.2091>.
- Guo, X. Y., L. Wang, L. Tian, and X. Li, 2017: Elevation-dependent reductions in wind speed over and around the Tibetan Plateau. *Int. J. Climatol.*, **37**, 1117–1126, <https://doi.org/10.1002/joc.4727>.
- He, Y., A. H. Monahan, and C. G. Jones, 2010: Probability distributions of land surface wind speeds over North America. *J. Geophys. Res.*, **115**, D04103, <https://doi.org/10.1029/2008JD010708>.
- , H. Tian, and W. T. Deng, 2012: Comparative analysis of the effects of different methods in homogeneity test on annual wind speed (in Chinese). *Daqi Kexue Xuebao*, **35**, 342–349.
- Hersbach, H., C. Peubey, A. Simmons, P. Berrisford, P. Poli, and D. Dee, 2015: ERA-20CM: A twentieth-century atmospheric model ensemble. *Quart. J. Roy. Meteor. Soc.*, **141**, 2350–2375, <https://doi.org/10.1002/qj.2528>.
- Higgins, R. W., A. Leetmaa, and V. E. Kousky, 2002: Relationships between climate variability and winter temperature extremes in the United States. *J. Climate*, **15**, 1555–1572, [https://doi.org/10.1175/1520-0442\(2002\)015<1555:RBCVAW>2.0.CO;2](https://doi.org/10.1175/1520-0442(2002)015<1555:RBCVAW>2.0.CO;2).
- Hirahara, S., M. Ishii, and Y. Fukuda, 2014: Centennial-scale sea surface temperature analysis and its uncertainty. *J. Climate*, **27**, 57–75, <https://doi.org/10.1175/JCLI-D-12-00837.1>.
- Huang, Y., B. Wang, X. Li, and H. Wang, 2018: Changes in the influence of the western Pacific subtropical high on Asian summer monsoon rainfall in the late 1900s. *Climate Dyn.*, **51**, 443–455, <https://doi.org/10.1007/s00382-017-3933-1>.
- Jekel, C., and G. Venter, 2019: pwlf: A Python library for fitting 1D continuous piecewise linear functions. GitHub, https://github.com/cjekel/piecewise_linear_fit_py.
- Jiang, Y., Y. Luo, Z. C. Zhao, and S. W. Tao, 2010: Changes in wind speed over China during 1956–2004. *Theor. Appl. Climatol.*, **99**, 421–430, <https://doi.org/10.1007/s00704-009-0152-7>.
- Jung, C., D. Schindler, and J. Laible, 2018: National and global wind resource assessment under six wind turbine installation scenarios. *Energy Convers. Manage.*, **156**, 403–415, <https://doi.org/10.1016/j.enconman.2017.11.059>.
- , D. Taubert, and D. Schindler, 2019: The temporal variability of global wind energy—Long-term trends and interannual variability. *Energy Convers. Manage.*, **188**, 462–472, <https://doi.org/10.1016/j.enconman.2019.03.072>.
- Kalnay, E., and M. Cai, 2003: Impact of urbanization and land-use change on climate. *Nature*, **423**, 528–531, <https://doi.org/10.1038/nature01675>.
- Kim, J. C., and K. Paik, 2015: Recent recovery of surface wind speed after decadal decrease: A focus on South Korea. *Climate Dyn.*, **45**, 1699–1712, <https://doi.org/10.1007/s00382-015-2546-9>.
- Laloyaux, R., and Coauthors, 2018: CERA-20C: A coupled reanalysis of the twentieth century. *J. Adv. Model. Earth Syst.*, **10**, 1172–1195, <https://doi.org/10.1029/2018MS001273>.
- Li, J. P., 2005: Coupled air–sea oscillations and climate variations in China. *Climate and Environmental Evolution in China*, Vol. 1, D. Qin, Ed., China Meteorological Press, 324–333.
- , and Q. C. Zeng, 2002: A unified monsoon index. *Geophys. Res. Lett.*, **29**, 1274, <https://doi.org/10.1029/2001GL013874>.
- , and J. X. L. Wang, 2003: A modified zonal index and its physical sense. *Geophys. Res. Lett.*, **30**, 1632, <https://doi.org/10.1029/2003GL017441>.
- , and Q. C. Zeng, 2003: A new monsoon index and the geographical distribution of the global monsoons. *Adv. Atmos. Sci.*, **20**, 299–302, <https://doi.org/10.1007/s00376-003-0016-5>.

- , J. Feng, and Y. Li, 2011: A possible cause of decreasing summer rainfall in northeast Australia. *Int. J. Climatol.*, **32**, 995–1005, <https://doi.org/10.1002/joc.2328>.
- Li, Q. X., X. N. Liu, H. Z. Zhang, and Q. P. Tu, 2003: Homogeneity study of situ observational climate series (in Chinese). *Mater. Sci. Technol.*, **31**, 3–10.
- Li, Y., Y. Wang, H. Y. Chu, and J. P. Tang, 2008: The climate influence of anthropogenic land-use changes on near-surface wind energy potential in China. *Chin. Sci. Bull.*, **53**, 2859–2866, <https://doi.org/10.1007/s11434-008-0360-z>.
- Li, Z. Q., and Coauthors, 2016: Aerosol and monsoon climate interactions over Asia. *Rev. Geophys.*, **54**, 866–929, <https://doi.org/10.1002/2015RG000500>.
- , L. L. Song, H. Ma, J. J. Xiao, K. Wang, and L. Chen, 2018: Observed surface wind speed declining induced by urbanization in East China. *Climate Dyn.*, **50**, 735–749, <https://doi.org/10.1007/s00382-017-3637-6>.
- Lim, Y. K., M. Cai, E. Kalnay, and L. Zhou, 2005: Observational evidence of sensitivity of surface climate changes to land types and urbanization. *Geophys. Res. Lett.*, **32**, L22712, <https://doi.org/10.1029/2005GL024267>.
- Lin, C. G., K. Yang, J. Qin, and Y. Hu, 2013: Observation coherent trends of surface and upper-air wind speed over China since 1960. *J. Climate*, **26**, 2891–2903, <https://doi.org/10.1175/JCLI-D-12-00093.1>.
- Liu, X., X. J. Zhang, Q. Tang, and X. Z. Zhang, 2014: Effect of surface wind speed decline on modeled hydrological conditions in China. *Hydrol. Earth Syst. Sci.*, **18**, 2803–2813, <https://doi.org/10.5194/hess-18-2803-2014>.
- Liu, X. N., 2000: The homogeneity test on mean annual wind speed over China (in Chinese). *Quart. J. Appl. Meteor.*, **11**, 28–34.
- Lu, R., X. W. Hong, and X. Y. Li, 2016: Asymmetric association of rainfall and atmospheric circulation over East Asia with anomalous rainfall in the tropical western North Pacific in summer. *Atmos. Ocean. Sci. Lett.*, **9**, 185–190, <https://doi.org/10.1080/16742834.2016.1161489>.
- Luo, M., J. M. Feng, Z. F. Xu, Y. L. Wang, and L. Dan, 2019: Evaluating the performance of five twentieth-century reanalysis datasets in reproducing the severe drought in northern China during the 1920s–1930s. *Theor. Appl. Climatol.*, **137**, 187–199, <https://doi.org/10.1007/s00704-018-2591-5>.
- Mantua, N. J., S. R. Hare, Y. Zhang, J. M. Wallace, and S. C. Francis, 1997: A Pacific interdecadal climate oscillation with impacts on salmon production. *Bull. Amer. Meteor. Soc.*, **78**, 1069–1080, [https://doi.org/10.1175/1520-0477\(1997\)078<1069:APICOW>2.0.CO;2](https://doi.org/10.1175/1520-0477(1997)078<1069:APICOW>2.0.CO;2).
- Mastylo, M., 2013: Bilinear interpolation theorems and applications. *J. Funct. Anal.*, **265**, 185–207, <https://doi.org/10.1016/j.jfa.2013.05.001>.
- McMahon, T. A., M. C. Peel, L. Lowe, R. Srikanthan, and T. R. McVicar, 2013: Estimating actual, potential, reference crop and pan evaporation using standard meteorological data: A pragmatic synthesis. *Hydrol. Earth Syst. Sci.*, **17**, 1331–1363, <https://doi.org/10.5194/hess-17-1331-2013>.
- McVicar, T. R., T. G. Van Niel, L. T. Li, M. L. Roderick, D. P. Rayner, L. Ricciardulli, and R. Donohue, 2008: Wind speed climatology and trends for Australia, 1975–2006: Capturing the stilling phenomenon and comparison with near-surface reanalysis output. *Geophys. Res. Lett.*, **35**, L20403, <https://doi.org/10.1029/2008GL035627>.
- , —, M. L. Roderick, L. T. Li, X. G. Mo, N. E. Zimmermann, and D. R. Schmatz, 2010: Observational evidence from two mountainous regions that near-surface wind speeds are declining more rapidly at higher elevations than lower elevations: 1960–2006. *Geophys. Res. Lett.*, **37**, L06402, <https://doi.org/10.1029/2009GL042255>.
- , and Coauthors, 2012: Global review and synthesis of trends in observed terrestrial near-surface wind speeds: Implications for evaporation. *J. Hydrol.*, **416–417**, 182–205, <https://doi.org/10.1016/j.jhydrol.2011.10.024>.
- Minola, L. C., C. Azorin-Molina, and D. Chen, 2016: Homogenization and assessment of observed near-surface wind speed trends across Sweden, 1956–2013. *J. Climate*, **29**, 7397–7415, <https://doi.org/10.1175/JCLI-D-15-0636.1>.
- Moen, J., and A. Brekke, 1993: The solar flux influence on quiet time conductances in the auroral ionosphere. *Geophys. Res. Lett.*, **20**, 971–974, <https://doi.org/10.1029/92GL02109>.
- Naizghi, M. S., and T. B. Ouarda, 2017: Teleconnections and analysis of long-term wind speed variability in the UAE. *Int. J. Climatol.*, **37**, 230–248, <https://doi.org/10.1002/joc.4700>.
- Nan, S. L., and J. P. Li, 2003: The relationship between the summer precipitation in the Yangtze River valley and the boreal spring Southern Hemisphere annular mode. *Geophys. Res. Lett.*, **30**, 2266, <https://doi.org/10.1029/2003GL018381>.
- Nchaba, T., M. Mpholo, and C. Lennard, 2017: Long-term austral summer wind speed trends over southern Africa. *Int. J. Climatol.*, **37**, 2850–2862, <https://doi.org/10.1002/joc.4883>.
- Ni, Y., L. Zhou, Y. Liu, A. Wu, G. Wang, X. Yang, and X. Zhang, 1995: Study for ENSO and its influences on Asian monsoon and climate change of China (in Chinese). *Sci. Meteor. Sinica*, **4**, 30–45.
- Niyogi, D., P. Pyle, M. Lei, S. P. Arya, C. M. Kishtawal, M. Shepherd, F. Chen, and B. Wolfe, 2011: Urban modification of thunderstorms: An observational storm climatology and model case study for the Indianapolis urban region. *J. Appl. Meteor. Climatol.*, **50**, 1129–1144, <https://doi.org/10.1175/2010JAMC1836.1>.
- Peterson, T. C., R. Vautard, T. R. McVicar, J. N. Thepaut, and P. Berrisford, 2011: Surface winds over land [in “State of the Climate in 2010”]. *Bull. Amer. Meteor. Soc.*, **92** (6), S57, <https://doi.org/10.1175/1520-0477-92.6.S1>.
- Poli, P., and Coauthors, 2013: The data assimilation system and initial performance evaluation of the ECMWF pilot reanalysis of the 20th-century assimilating surface observations only (ERA-20c). ERA Rep. Series 14, 59 pp., <https://www.ecmwf.int/node/11699>.
- , and Coauthors, 2016: ERA-20C: An atmospheric reanalysis of the twentieth century. *J. Climate*, **29**, 4083–4097, <https://doi.org/10.1175/JCLI-D-15-0556.1>.
- Ramon, J., L. Lledo, V. Torralba, A. Soret, and F. J. Doblas-Reyes, 2019: What global reanalysis best represents near-surface winds? *Quart. J. Roy. Meteor. Soc.*, **145**, 3236–3251, <https://doi.org/10.1002/qj.3616>.
- Rasmusson, E. M., and T. H. Carpenter, 1982: Variations in tropical sea surface temperature and surface wind fields associated with the Southern Oscillation/El Niño. *Mon. Wea. Rev.*, **110**, 354–384, [https://doi.org/10.1175/1520-0493\(1982\)110<0354:VITSST>2.0.CO;2](https://doi.org/10.1175/1520-0493(1982)110<0354:VITSST>2.0.CO;2).
- Roderick, M. L., L. D. Rotstayn, G. D. Farquhar, and M. T. Hobbins, 2007: On the attribution of changing pan evaporation. *Geophys. Res. Lett.*, **34**, L17403, <https://doi.org/10.1029/2007GL031166>.
- Sen, P. K., 1968: Estimates of the regression coefficients based on Kendall’s tau. *J. Amer. Stat. Assoc.*, **63**, 1379–1389, <https://doi.org/10.1080/01621459.1968.10480934>.
- Storn, R., and K. Price, 1997: Differential evolution—A simple and efficient heuristic for global optimization over continuous

- spaces. *J. Global Optim.*, **11**, 341–359, <https://doi.org/10.1023/A:1008202821328>.
- Tao, S., C. Fu, Z. Zeng, Q. Zhang, and D. Kaiser, 1997: Two long-term instrumental climatic data bases of the People's Republic of China. Oak Ridge National Laboratory ORNL/CDIAC-47, <https://cdiac.ess-dive.lbl.gov/epubs/ndp/ndp039/ndp039.html>.
- Thiel, H., 1950: A rank-invariant method of linear and polynomial analysis, Part III. *Ned. Akad. Wet. Proc.*, **53**, 1397–1412.
- Thomas, B. R., and V. R. Swail, 2011: Buoy wind inhomogeneities related to averaging method and anemometer type: Application to long time series. *Int. J. Climatol.*, **31**, 1040–1055, <https://doi.org/10.1002/joc.2339>.
- Thompson, D. W. J., and J. M. Wallace, 1998: The Arctic Oscillation signature in the wintertime geopotential height and temperature fields. *Geophys. Res. Lett.*, **25**, 1297–1300, <https://doi.org/10.1029/98GL00950>.
- Tobin, I., P. Berrisford, R. J. H. Dunn, R. Vautard, and T. R. McVicar, 2014: Land surface wind speed [in “State of the Climate in 2013”]. *Bull. Amer. Meteor. Soc.*, **95**, S28–S29, <https://doi.org/10.1175/2014BAMSStateoftheClimate.1>.
- Torrallba, V., F. J. Doblas-Reyes, and N. Gonzalez-Reviriego, 2017: Uncertainty in recent near-surface wind speed trends: A global reanalysis intercomparison. *Environ. Res. Lett.*, **12**, 114019, <https://doi.org/10.1088/1748-9326/aa8a58>.
- Trenberth, K. E., 1997: The definition of El Niño. *Bull. Amer. Meteor. Soc.*, **78**, 2771–2777, [https://doi.org/10.1175/1520-0477\(1997\)078<2771:TDOENO>2.0.CO;2](https://doi.org/10.1175/1520-0477(1997)078<2771:TDOENO>2.0.CO;2).
- , and D. P. Stepaniak, 2001: Indices of El Niño evolution. *J. Climate*, **14**, 1697–1701, [https://doi.org/10.1175/1520-0442\(2001\)014<1697:LIOENO>2.0.CO;2](https://doi.org/10.1175/1520-0442(2001)014<1697:LIOENO>2.0.CO;2).
- Vautard, R., J. L. Cattiaux, P. Yiou, J. N. Thepaut, and P. Ciais, 2010: Northern Hemisphere atmospheric stilling partly attributed to an increase in surface roughness. *Nat. Geosci.*, **3**, 756–761, <https://doi.org/10.1038/ngeo979>.
- Wang, B., R. Wu, and K. M. Lau, 2001: Interannual variability of the Asian summer monsoon: Contrasts between the Indian and the western North Pacific–East Asian monsoons. *J. Climate*, **14**, 4073–4090, [https://doi.org/10.1175/1520-0442\(2001\)014<4073:IVOTAS>2.0.CO;2](https://doi.org/10.1175/1520-0442(2001)014<4073:IVOTAS>2.0.CO;2).
- Wang, C., and D. B. Enfield, 2001: The tropical Western Hemisphere warm pool. *Geophys. Res. Lett.*, **28**, 1635–1638, <https://doi.org/10.1029/2000GL011763>.
- Wang, J., J. M. Feng, Z. W. Yan, Y. Qiu, and L. J. Cao, 2020: An analysis of the urbanization contribution to observed terrestrial stilling in the Beijing–Tianjin–Hebei region of China. *Environ. Res. Lett.*, **15**, 034062, <https://doi.org/10.1088/1748-9326/ab7396>.
- Wang, L., 2014: An intensity index for the East Asian winter monsoon. *J. Climate*, **27**, 2361–2374, <https://doi.org/10.1175/JCLI-D-13-00086.1>.
- Wohland, J., N. E. Omrani, D. Witthaut, and N. S. Keenlyside, 2019: Inconsistent wind speed trends in current twentieth century reanalysis. *J. Geophys. Res. Atmos.*, **124**, 1931–1940, <https://doi.org/10.1029/2018JD030083>.
- Wu, J., J. L. Zha, and D. M. Zhao, 2016: Estimating the impact of the changes in land use and cover on the surface wind speed over the East China Plain during the period 1980–2011. *Climate Dyn.*, **46**, 847–863, <https://doi.org/10.1007/s00382-015-2616-z>.
- , —, —, and Q. D. Yang, 2018a: Changes in terrestrial near-surface wind speed and their possible causes: An overview. *Climate Dyn.*, **51**, 2039–2078, <https://doi.org/10.1007/s00382-017-3997-y>.
- , —, —, and —, 2018b: Changes of wind speed at different heights over eastern China during 1980–2011. *Int. J. Climatol.*, **38**, 4476–4495, <https://doi.org/10.1002/joc.5681>.
- , —, —, and —, 2018c: Effects of surface friction and turbulent mixing on long-term changes in the near-surface wind speed over the Eastern China Plain from 1981–2010. *Climate Dyn.*, **51**, 2285–2299, <https://doi.org/10.1007/s00382-017-4012-3>.
- Xu, M., C. P. Chang, C. B. Fu, Y. Qi, A. Robock, D. Robinson, and H. M. Zhang, 2006: Steady decline of East Asian monsoon winds, 1969–2000: Evidence from direct ground measurements of wind speed. *J. Geophys. Res.*, **111**, D24111, <https://doi.org/10.1029/2006JD007337>.
- Yang, X. M., and Coauthors, 2012: The decreasing wind speed in southwestern China during 1969–2009, and possible causes. *Quat. Int.*, **263**, 71–84, <https://doi.org/10.1016/j.quaint.2012.02.020>.
- You, Q. L., S. C. Kang, W. A. Flugel, N. Pepin, Y. P. Yan, and J. Huang, 2010: Decreasing wind speed and weakening latitudinal surface pressure gradients in the Tibetan Plateau. *Climate Res.*, **42**, 57–64, <https://doi.org/10.3354/cr00864>.
- Zeng, Z. Z., and Coauthors, 2019: A reversal in global terrestrial stilling and its implications for wind energy production. *Nat. Climate Change*, **9**, 979–985, <https://doi.org/10.1038/s41558-019-0622-6>.
- Zha, J. L., J. Wu, and D. M. Zhao, 2016: Changes of probabilities in different wind grades induced by land use and cover change in Eastern China Plain during 1980–2011. *Atmos. Sci. Lett.*, **17**, 264–269, <https://doi.org/10.1002/asl.653>.
- , —, and —, 2017: Effects of land use and cover change on the near-surface wind speed over China in the last 30 years. *Prog. Phys. Geogr.*, **41**, 46–67, <https://doi.org/10.1177/0309133316663097>.
- , —, —, and J. P. Tang, 2019a: A possible recover of the near-surface wind speed in Eastern China during winter after 2000 and the potential causes. *Theor. Appl. Climatol.*, **136**, 119–134, <https://doi.org/10.1007/s00704-018-2471-z>.
- , D. M. Zhao, J. Wu, and P. W. Zhang, 2019b: Numerical simulation of the effects of land use and cover change on the near-surface wind speed over Eastern China. *Climate Dyn.*, **53**, 1783–1803, <https://doi.org/10.1007/s00382-019-04737-w>.
- , J. Wu, D. M. Zhao, and W. X. Fan, 2020: Future projections of the near-surface wind speed over Eastern China based on CMIP5 datasets. *Climate Dyn.*, **54**, 2361–2385, <https://doi.org/10.1007/s00382-020-05118-4>.
- , D. M. Zhao, J. Wu, and C. Shen, 2021: Research progress and prospects of terrestrial near-surface wind speed variations in China. *J. Meteor. Res.*, **35**, 1–12, <https://doi.org/10.1007/s13351-021-0143-x>.
- Zhang, A. Y., G. Y. Ren, J. Guo, and Y. Wang, 2009: Change trend analyses on Upper-air wind speed over China in past 30 years (in Chinese). *Plateau Meteor.*, **28**, 680–687.
- Zhang, G. F., and Coauthors, 2020: Variability of daily maximum wind speed across China, 1975–2016: An examination of likely causes. *J. Climate*, **33**, 2793–2816, <https://doi.org/10.1175/JCLI-D-19-0603.1>.
- Zhang, L., T. Li, and M. M. Lu, 2017: Surface wind energy near Taiwan in winter since 1871. *Terr. Atmos. Ocean. Sci.*, **28**, 295–302, [https://doi.org/10.3319/TAO.2016.04.29.01\(A\)](https://doi.org/10.3319/TAO.2016.04.29.01(A)).
- Zhang, N., X. M. Wang, Y. Chen, W. Dai, and X. Y. Wang, 2015: Numerical simulations on influence of urban land cover expansion and anthropogenic heat release on urban meteorological environment in Pearl River Delta. *Theor. Appl. Climatol.*, **126**, 469–479, <https://doi.org/10.1007/s00704-015-1601-0>.

- Zhang, Y., S. P. Xie, Y. Kosaka, and J. C. Yang, 2018: Pacific decadal oscillation: Tropical Pacific forcing versus internal variability. *J. Climate*, **31**, 8265–8279, <https://doi.org/10.1175/JCLI-D-18-0164.1>.
- Zhang, Z. T., and K. C. Wang, 2020: Stilling and recovery of the surface wind speed based on observation, reanalysis, and geostrophic wind theory over China from 1960 to 2017. *J. Climate*, **33**, 3989–4008, <https://doi.org/10.1175/JCLI-D-19-0281.1>.
- , ———, D. L. Chen, J. P. Li, and R. Dickinson, 2019: Increase in surface friction dominates the observed surface wind speed decline during 1973–2014 in the Northern Hemisphere lands. *J. Climate*, **32**, 7421–7435, <https://doi.org/10.1175/JCLI-D-18-0691.1>.
- Zheng, H., X. Liu, C. Liu, X. Dai, and R. Zhu, 2009: Assessing contribution to pan evaporation trends in Haihe River basin, China. *J. Geophys. Res.*, **114**, D24105, <https://doi.org/10.1029/2009JD012203>.